

Global Characteristics of X-Ray Flashes and X-Ray-Rich GRBs Observed by HETE-2

T. Sakamoto^{1,2}, D. Q. Lamb⁴, C. Graziani⁴, T. Q. Donaghy⁴, M. Suzuki¹, G. Ricker⁵, J-L. Atteia⁶, N. Kawai^{1,2}, A. Yoshida^{2,7}, Y. Shirasaki⁸, T. Tamagawa², K. Torii¹⁹, M. Matsuoka⁹, E. E. Fenimore³, M. Galassi³, J. Doty⁵, R. Vanderspek⁵, G. B. Crew⁵, J. Villasenor⁵, N. Butler⁵, G. Prigozhin⁵, J. G. Jernigan¹¹, C. Barraud⁶, M. Boer¹², J-P. Dezalay¹², J-F. Olive¹², K. Hurley¹¹, A. Levine⁵, G. Monnelly⁵, F. Martel⁵, E. Morgan⁵, S. E. Woosley¹³, T. Cline¹⁴, J. Braga¹⁵, R. Manchanda¹⁶, G. Pizzichini¹⁷, K. Takagishi¹⁸, and M. Yamauchi¹⁸

ABSTRACT

We describe and discuss the global properties of 45 gamma-ray bursts (GRBs) observed by HETE-2 during the first three years of its mission, focusing on the properties of X-Ray Flashes (XRFs) and X-ray-rich GRBs (XRRs). We find that the numbers of XRFs, XRRs, and GRBs are comparable. We find that the

¹Department of Physics, Tokyo Institute of Technology, 2-12-1 Ookayama, Meguro-ku, Tokyo 152-8551, Japan

²RIKEN (Institute of Physical and Chemical Research), 2-1 Hirosawa, Wako, Saitama 351-0198, Japan

³Los Alamos National Laboratory, P.O. Box 1663, Los Alamos, NM, 87545

⁴Department of Astronomy and Astrophysics, University of Chicago, IL, 60637

⁵Center for Space Research, Massachusetts Institute of Technology, 70 Vassar Street, Cambridge, MA, 02139

⁶Laboratoire d'Astrophysique, Observatoire Midi-Pyrénées, 14 Ave. E. Belin, 31400 Toulouse, France

⁷Department of Physics, Aoyama Gakuin University, Chitosedai 6-16-1, Setagaya-ku, Tokyo 157-8572, Japan

⁸National Astronomical Observatory, Osawa 2-21-1, Mitaka, Tokyo 181-8588, Japan

⁹Tsukuba Space Center, National Space Development Agency of Japan, Tsukuba, Ibaraki, 305-8505, Japan

¹⁰Department of Astronomy, New Mexico State University, 1320 Frenger Mall, Las Cruces, NM, 88003-8001

¹¹University of California at Berkeley, Space Sciences Laboratory, Berkeley, CA, 94720-7450

¹²Centre d'Etude Spatiale des Rayonnements, CNRS/UPS, B.P.4346, 31028 Toulouse Cedex 4, France

¹³Department of Astronomy and Astrophysics, University of California at Santa Cruz, 477 Clark Kerr Hall, Santa Cruz, CA 95064

¹⁴NASA Goddard Space Flight Center, Greenbelt, MD, 20771

¹⁵Instituto Nacional de Pesquisas Espaciais, Avenida Dos Astronautas 1758, Saõ José dos Campos 12227-010, Brazil

¹⁶Department of Astronomy and Astrophysics, Tata Institute of Fundamental Research, Homi Bhabha Road, Mumbai, 400 005, India

¹⁷IASF/CNR Sezione di Bologna, via Gobetti 101, 40129 Bologna Italy

¹⁸Faculty of engineering, Miyazaki University, Gakuen Kibanadai Nishi, Miyazaki 889-2192, Japan

¹⁹Department of Earth and Space Science, Graduate School of Science, Osaka University, 1-1 Machikaneyama-cho, Toyonaka, Osaka, 560-0043, Japan

durations and the sky distributions of XRFs and XRRs are similar to those of GRBs. We also find that the spectral properties of XRFs and XRRs are similar to those of GRBs, except that the values of the peak energy $E_{\text{peak}}^{\text{obs}}$ of the burst spectrum in νF_{ν} , the peak energy flux F_{peak} , and the energy fluence S_E of XRFs are much smaller – and those of XRRs are smaller – than those of GRBs. Finally, we find that the distributions of all three kinds of bursts form a continuum in the $[S_E(2\text{-}30\text{ keV}), S_E(30\text{-}400\text{ keV})]$ -plane, the $[S_E(2\text{-}400\text{ keV}), E_{\text{peak}}]$ -plane, and the $[F_{\text{peak}}(50\text{-}300\text{ keV}), E_{\text{peak}}]$ -plane. These results provide strong evidence that all three kinds of bursts arise from the same phenomenon.

Subject headings: Gamma rays: bursts

1. Introduction

Gamma-ray bursts (GRBs) whose energy fluence S_X in the X-ray energy band (2-30 keV) is larger than their energy fluence S_{γ} in the gamma-ray energy band (30-400 keV) have received increasing attention over the last few years. In particular, the Wide Field Camera (WFC) on *BeppoSAX* detected events that were not detected by the Gamma-Ray Burst Monitor (GRBM) on the same satellite. These events have been termed “X-ray flashes” (XRFs) (Heise et al. 2000). Events for which the ratio of the fluence in the X-ray energy band is intermediate between those for XRFs and GRBs have been termed “X-ray-rich GRBs” (XRRs).¹ Understanding the relationship between XRFs, XRRs, and GRBs may provide a deeper understanding of the prompt emission of GRBs.

2. Observations

In this paper, we investigate the global properties of a sample of HETE-2 bursts. We require the bursts in this sample to satisfy the following criteria: (1) the burst is detected in the WXM, (2) the burst is localizable by the WXM, and (3) the signal-to-noise of the WXM data is sufficient to carry out a spectral analysis of the burst. Generally, a joint spectral analysis is carried out for the WXM and the FREGATE data.

Forty-five bursts observed by HETE-2 between the beginning of the HETE-2 mission and 2003 September 13 met these criteria, and this is the sample of bursts that we study.

¹Throughout this paper, we define “X-ray-rich” GRBs (XRRs) and “X-ray flashes” (XRFs) as those events for which $\log[S_X(2 - 30\text{ keV})/S_{\gamma}(30 - 400\text{ keV})] > -0.5$ and 0.0 , respectively.

In this study, we consider three spectral models: (1) a power law (PL) model whose two parameters are the power-law index α and the normalization constant K_{15} of the spectrum at 15 keV; (2) a power law times exponential (PLE) model whose three parameters are the power-law index α , the cutoff energy E_0 , and K_{15} ; and (3) the Band function (Band et al. 1993) whose four parameters are the low-energy power-law index α , the cutoff energy E_0 , the high-energy power-law index β , and K_{15} . We determine whether the data requests a more complicated model (e.g., the PLE model instead of the PL model, or the Band function instead of the PLE model) using the maximum likelihood ratio test, and require a significance $Q < 10^{-2}$ in order to adopt the more complicated model.

Table 1 gives some information about the localization and the WXM time histories of the 45 bursts in the sample. Table 2 gives the details of the fits made to the time-averaged spectral data for each of the bursts, including the class of the burst (e.g., XRF, XRR, GRB) and the spectral parameters of the best-fit spectral model. Table 3 gives the photon number and energy fluence of each burst in the 2-30, 30-400, and 2-400 keV energy bands, and also energy fluence ratio between 2-30 keV and 30-400 keV. Table 4 gives the photon number peak flux (1 second) of each burst in 2-30 keV, 30-400 keV, 2-400 keV and 50-300 keV (BATSE Channels 3 and 4; Paciasas et al. (1999)) bands.

When the WXM photon time- and energy-tagged data (TAG data) are available, we apply a “cut” to the WXM data using only the photons from the pixels on wires in the X and Y detectors that were illuminated by the burst and that maximize the signal-to-noise ratio (S/N), in the same manner as we did for GRB 020531 (Lamb et al. 2004a). We used the spectral survey data (PHA data for WXM, and SP data for FREGATE), when TAG data are not available. The WXM and FREGATE detector response matrix has been well-calibrated using observations of the Crab nebula (WXM; Shirasaki et al. (2003), FREGATE; Olive et al. (2003)). We use the XSPEC version 11.2.0 software package to do the spectral fits. Details of instruments are given in Kawai et al. (2003) and Shirasaki et al. (2003) for the WXM, and in Atteia et al. (2003) for the FREGATE.

The time histories of the bursts, details of the spectral fitting procedure, and time-resolved spectroscopy of some of the bursts are given in a companion paper (Sakamoto et al 2004b; see also Lamb et al. 2004b). Other information about the bursts, including skymaps of the HETE-2 WXM and SXC localizations; the FREGATE T_{50} and T_{90} durations of the bursts; whether an X-ray, optical, or radio afterglow was detected; whether a host galaxy has been identified; and the redshift of the burst can be found in the First HETE-2 Burst Catalog (Vanderspek et al. 2004).

3. X-ray and γ -ray Fluences

3.1. Distribution of Ratio of X-ray and γ -ray Fluences

The distribution of the fluence ratio S_X (2-30 keV)/ S_γ (30-400 keV) for the 45 bursts in this study is shown in Figure 1. The boundaries between GRBs and XRRs, and XRRs and XRFs are shown as dashed lines. The Figure clearly shows that XRFs, XRRs, and GRBs form a single broad distribution. The numbers of XRFs, XRRs, and GRBs, are 16, 19, and 10, respectively. The numbers of all three kinds of bursts are roughly equal, modulo the relatively small sample size.

3.2. S_X versus S_γ

Figure 2 shows the distributions of XRFs, XRRs, and GRBs in the [S_E (2-30 keV), S_E (30–400 keV)]-plane. As was evident in Figure 1, the three GRB classes seem to form a single distribution. There is a strong, tight positive correlation between S_E (2-30 keV) and S_E (30-400 keV): $S_E(30-400 \text{ keV}) = (0.722 \pm 0.161) \times S_E(2-30 \text{ keV})^{1.282 \pm 0.082}$. The tightness of the correlation implies that there are no bursts in the HETE-2 sample with a high X-ray fluence and a low γ -ray fluence, or vice versa.

4. Durations

Figure 3 shows the distribution of T_{50} (top panel) and T_{90} (bottom panel) in the WXM energy band (2-25 keV) for each kind of GRB. For comparison, we also show the distribution of T_{50} and T_{90} for the BATSE bursts (Paciesas et al. 1999). Although the energy bands in which T_{50} and T_{90} are calculated are different for HETE-2 and BATSE, the distribution of the durations of the HETE-2 GRBs are consistent with the distribution of the durations of the BATSE long GRBs. There is also no evidence for any difference in the distribution of durations between the three kinds of GRBs. This result is consistent with the *BeppoSAX* WFC/CGRO BATSE sample of XRFs (Kippen et al. 2002).

5. Sky Distributions

Figure 4 shows the sky distribution in ecliptic coordinates of HETE-2 XRFs, XRRs, and GRBs (upper three panels), and of all of the 44 HETE-2 bursts ² in this study (bottom panel). The HETE-2 sky coverage is not uniform, and as a result, it is difficult to make a meaningful statement about the sky distributions of these three kinds of GRBs. Modulo this and the relatively small sample size of each of the three kinds of bursts, there is no statistically significant evidence that the sky distributions of the three kinds of bursts are different.

6. Distribution of Spectral Parameters

We find that a simple PL model provides an adequate fit to the spectral data for eight of the 45 bursts in this study. Six of these bursts are XRFs and two are XRRs. In the case of the five XRFs, the slope of the power-law index is < -2 . We interpret that the spectral data for these bursts do not constrain $E_{\text{peak}}^{\text{obs}}$ but the fact that $\beta < -2$ means that $E_{\text{peak}}^{\text{obs}}$ is about 2 keV. This energy is near or below the lower limit of the WXM energy band. Therefore, we are observing the high-energy power-law portion of their Band spectrum and they are XRFs. In the case of the four XRRs, the normalization constants K_{15} of the spectra are the lowest among all of the XRRs and GRBs. We therefore interpret the lack of evidence for $E_{\text{peak}}^{\text{obs}}$ in these bursts as due to the low signal-to-noise of their spectra. In this case, it is difficult to constrain the break energy, E_0 , of the spectra and the best representable spectral model will be a simple power-law.

We find that the PLE model provides an adequate fit to the spectral data for 28 of the 45 bursts in this study. Eight of these bursts are XRFs, thirteen are XRRs, and six are GRBs. The remaining ten bursts in this study are adequately fit by the Band model but not by any simpler model.

We do not include two GRBs (GRB020813 and GRB030519) with $\beta > -2$ in this study, because they do not represent actual “peak” energy in νF_ν spectrum.

²Since the attitude control camera was not operational, the celestial coordinates of GRB010225 is not available.

6.1. Distribution of α -Values

Figure 5 shows the distribution of the low-energy photon index α . We include in this figure bursts which require the PLE model or the Band model in order to adequately represent their energy spectra. We do not include bursts whose spectra are adequately represented by a simple PL model, since in this case the photon index of the PL model is most likely the high-energy photon index β of the Band model. There is a well-known systematic effect when fitting the PLE model to a spectrum whose shape is that of the Band model but for which the energy range or the signal-to-noise of the observations is insufficient to require the Band model: the low-energy power-law index α is smaller (more negative) than it would otherwise be, and the peak energy $E_{\text{peak}}^{\text{obs}}$ of the spectrum in νF_{ν} is larger than it would otherwise be. This systematic effect must be kept in mind when comparing bursts for which the PLE model adequately represents the data and bursts for which the Band model is required to adequately represent the data. We therefore show as hatched the α -values for burst spectra requiring the Band model and as non-hatched the α -values for burst spectra that are adequately fit by the PLE model. However, there is no clear evidence in Figure 5 of the above systematic effect.

The distribution of the low-energy photon index α clusters around -1 , and is similar to the BATSE distribution of α values (Preece et al. 2000). The relatively small number of bursts with $\alpha > -0.5$ in the HETE-2 burst sample compared to the BATSE sample of bright bursts (Preece et al. 2000) could be due to three reasons: (1) the HETE-2 burst sample might be lacking very hard GRBs because such bursts are relatively more difficult for the WXM to detect and to localize, (2) the HETE-2 values are for time-averaged burst spectra whereas the α values reported for the BATSE sample of bright bursts by (Preece et al. 2000) are for time-resolved spectra; and (3) the PLE model provides an adequate fit to the spectra of most of the HETE-2 bursts, and therefore the value of α is systematically more negative than it would otherwise be, as mentioned above. The first reason is unlikely because very hard GRBs are also very intense (i.e., they have large peak fluxes and fluences). The second reason may play a role, since it is well known that the spectra of most bursts are hardest at or near the peak of the burst time history and softer afterward. We regard the third reason as the most likely, since the vast majority of the 5000 time-resolved burst spectra in the BATSE sample required the Band model in order to adequately fit the spectrum.

There are no statistically significant differences between the distributions of α values for XRFs, XRRs, and GRBs (see the top three panels of Figure 5), although comparison of the three distributions suffers from small number statistics and from the presence of the above systematic effect. Nevertheless, we conclude that there is no evidence that the distribution of α -values for XRFs, XRRs, and GRBs are different.

6.2. Distribution of $E_{\text{peak}}^{\text{obs}}$ -Values

Figure 6 shows the distribution of the observed peak energy $E_{\text{peak}}^{\text{obs}}$ of the burst spectra in νF_{ν} . The events labeled with left-pointing arrows are the 99.7% upper limits for $E_{\text{peak}}^{\text{obs}}$ derived using the *constrained* Band function (Sakamoto et al. 2004a). The distribution of $E_{\text{peak}}^{\text{obs}}$ is clearly distorted by the systematic effect mentioned above; i.e., bursts for which the PLE model provides an adequate representation of the data have values of $E_{\text{peak}}^{\text{obs}}$ that are larger than they would otherwise be. Despite this systematic effect, the distribution of $E_{\text{peak}}^{\text{obs}}$ values for the sample of HETE-2 GRBs is much broader than that for the BATSE sample of time-resolved spectra of bright bursts (Preece et al. 2000). In particular, the distribution of $E_{\text{peak}}^{\text{obs}}$ values in the HETE-2 burst sample extends to much lower energies. There are clear differences between the $E_{\text{peak}}^{\text{obs}}$ distributions for XRFs, XRRs, and GRBs, but this is simply because of the strong correlation that must exist between $E_{\text{peak}}^{\text{obs}}$ and the fluence ratio $S_E(2-30 \text{ keV})/S_E(30-400 \text{ keV})$. This is the fact that we are classifying the GRBs for 30 keV as a boundary. The E_{peak} distributions of the XRRs and the hard GRBs are quite similar.

The distribution of β is shown in Figure 7. Because of the small number of GRBs with significantly constrained β , only the distribution for all the GRB classes are plotted. The distribution of β is similar to the BATSE GRBs (Preece et al. 2000).

7. Correlations Between $E_{\text{peak}}^{\text{obs}}$ and Other Burst Properties

7.1. $E_{\text{peak}}^{\text{obs}}$ vs. Fluence Ratio

Figure 8 shows the distribution of observed peak energy $E_{\text{peak}}^{\text{obs}}$ versus the fluence ratio $S_E(2-30 \text{ keV})/S_E(30-400 \text{ keV})$. Since the fluence ratio is independent of the normalization parameter of the model spectrum, it is possible to calculate the relationship between the fluence ratio and $E_{\text{peak}}^{\text{obs}}$. The overlaid curves in Figure 8 are the calculated relationships, assuming the Band function, for $\alpha = -1$ and $\beta = -2.5$ (red), -3.0 (blue), and -20.0 (green). The dependence of the fluence ratio on β is weak when $E_{\text{peak}}^{\text{obs}}$ is greater than 30 keV, and understandably, becomes strong when $E_{\text{peak}}^{\text{obs}}$ is less than 30 keV. This implies that the choice of the proper spectral model is important for determining the fluence ratio, and for determining which bursts are XRFs and XRRs. Fortunately, the importance of choosing the correct spectral model for the latter is modest because a range in β of (-2) - (-20) produces a range in the fluence ratio of only 40% at $E_{\text{peak}}^{\text{obs}} = 30 \text{ keV}$, which corresponds to the boundary between XRFs and XRRs.

7.2. α and β vs. $E_{\text{peak}}^{\text{obs}}$

Figure 9 shows the distribution of α -values (left panel) and β -values (right panel) versus $E_{\text{peak}}^{\text{obs}}$. α and β show no statistically significant correlation with $E_{\text{peak}}^{\text{obs}}$, and therefore none with the kind of burst. Kippen et al. (2002) also found no statistically significant correlation between α and $E_{\text{peak}}^{\text{obs}}$ in the *BeppoSAX* WFC/CGRO BATSE sample of XRFs and GRBs.

7.3. 2-400 keV Fluence vs. $E_{\text{peak}}^{\text{obs}}$

The correlation between the fluence in 2–400 keV and $E_{\text{peak}}^{\text{obs}}$ are shown in Figure 10. This figure shows the correlation between $S_E(2\text{--}400\text{ keV})$ and $E_{\text{peak}}^{\text{obs}}$. The best-fit power-law slope between $E_{\text{peak}}^{\text{obs}}$ and $S_E(2\text{--}400\text{ keV})$ is 0.279 ± 0.053 . Thus, while the scatter in the correlation is large (the correlation coefficient is 0.511), the significance of the correlation is also large.

7.4. Peak Photon Number Flux vs. $E_{\text{peak}}^{\text{obs}}$

Figures 11 and 12 show the distribution of HETE-2 bursts in the $[F_N^{\text{P}}(2\text{--}400\text{ keV}), E_{\text{peak}}^{\text{obs}}]$ -plane and the $[F_N^{\text{P}}(50\text{--}300\text{ keV}), E_{\text{peak}}^{\text{obs}}]$ -plane, respectively. There is no evidence for a correlation between $E_{\text{peak}}^{\text{obs}}$ and the peak photon flux $F_N^{\text{P}}(2\text{--}400\text{ keV})$, while a strong correlation exists between $E_{\text{peak}}^{\text{obs}}$ and the peak photon flux $F_N^{\text{P}}(50\text{--}300\text{ keV})$ (the latter has a correlation coefficient of 0.802). Kippen et al. (2002) suggested a similar correlation for the WFC/BATSE sample of XRFs and GRBs.

However, the correlation between $E_{\text{peak}}^{\text{obs}}$ and $F_N^{\text{P}}(50\text{--}300\text{ keV})$ is an artifact of the choice of 50–300 keV for the energy band in which the peak flux is measured. The reason is that for GRBs $F_N^{\text{P}}(50\text{--}300\text{ keV})$ is roughly the *bolometric* peak photon number flux, whereas for XRRs, and especially for XRFs, $F_N^{\text{P}}(50\text{--}300\text{ keV})$ it is clearly not. This is because $E_{\text{peak}}^{\text{obs}}$ lies near or below the lower limit of this energy band for XRRs, and far below the lower limit of the energy band for XRFs. The result is that the peak photon number fluxes for these bursts are greatly reduced from their bolometric values, as can be clearly seen by comparing Figures 11 and 12.

Figures 13 and 14 compare the distribution of HETE-2 bursts in the $[F_N^{\text{P}}(50\text{--}300\text{ keV}), E_{\text{peak}}^{\text{obs}}]$ -plane with the distribution of BATSE bursts and the distribution of WFC/BATSE bursts, respectively, in the same plane. The distribution of HETE-2 bursts is consistent with the distribution of BATSE bursts for $E_{\text{peak}}^{\text{obs}} > 50\text{ keV}$ but extends farther down in $E_{\text{peak}}^{\text{obs}}$ (and

therefore in $F_N^P(50-300 \text{ keV})$). This is expected because of the BATSE trigger threshold, which is 50 keV. The distribution of HETE-2 bursts is consistent with the distribution of WFC/BATSE bursts but also extends down to fainter peak photon number fluxes for a similar reason.

8. Discussion

8.1. Comparison of XRF, XRR, and GRB Properties

We have studied the global properties of 45 GRBs localized by the HETE-2 WXM during the first three years of its mission, focusing on the properties of XRFs and XRRs. We find that the numbers of XRFs, XRRs, and GRBs are comparable for bursts localized by the HETE-2 WXM. We find that there is no statistically significant evidence for any difference in the duration distributions or the sky distributions of the three kinds of bursts. We also find that the spectral properties of XRFs and XRRs are similar to those of GRBs, except that the values of the peak energy $E_{\text{peak}}^{\text{obs}}$ of the burst spectrum in νF_ν , the peak flux F_{peak} , and the fluence S_E of XRFs are much smaller – and those of XRRs are smaller – than those of GRBs. Our results are consistent with Barraud et al. (2003) who studied the spectral properties of the HETE-2 GRBs using the FREGATE data. Figure 15, which shows the best-fit νF_ν spectra of two XRFs, two XRRs, and two GRBs, illustrates this. Finally, we find that the distributions of all three kinds of bursts form a continuum in the $[S(2-30 \text{ keV}), S(30-400 \text{ keV})]$ -plane, the $[S(2-400 \text{ keV}), E_{\text{peak}}]$ -plane, and the $[F_{\text{peak}}(50-300 \text{ keV}), E_{\text{peak}}^{\text{obs}}]$ -plane. These results provide strong evidence that all three kinds of bursts arise from the same phenomenon.

8.2. Theoretical Models of XRFs

Several theoretical models of XRFs have been proposed. GRBs at very high redshifts might be observed as XRFs (Heise et al. 2000). However, the fact that the duration distribution for XRFs is similar to that for GRBs argues against this hypothesis as the explanation of most XRFs, as does the low redshifts (Soderberg et al. 2004; Fynbo et al. 2004) and the redshift constraints (Bloom et al. 2003) that exist for several XRFs.

According to Mészáros, Ramirez-Ruiz, Rees, & Zhang (2002) and Woosley, Zhang, & Heger (2003), X-ray (20-100 keV) photons are produced effectively by the hot cocoon surrounding the GRB jet as it breaks out, and could produce XRF-like events if viewed well off the axis of the jet. However, it is not clear that such a model would produce roughly

equal numbers of XRFs, XRRs, and GRBs, or the nonthermal spectra exhibited by XRFs.

Yamazaki et al. (2002, 2003) have proposed that XRFs are the result of a highly collimated GRB jet viewed well off the axis of the jet. In this model, the low values of E_{peak} and E_{iso} (and therefore for $E_{\text{peak}}^{\text{obs}}$ and S_E) seen in XRFs is the result of relativistic beaming. However, it is not clear that such a model can produce roughly equal numbers of XRFs, XRRs, and GRBs, and still satisfy the observed relation between E_{iso} and E_{peak} (Amati et al. 2002; Lamb et al. 2004b).

The “dirty fireball” model of XRFs posits that baryonic material is entrained in the GRB jet, resulting in a bulk Lorentz factor $\Gamma \ll 300$ (Dermer et al. 1999; Huang et al. 2002; Dermer and Mitman 2003). At the opposite extreme, GRB jets in which the bulk Lorentz factor $\Gamma \gg 300$ and the contrast between the bulk Lorentz factors of the colliding relativistic shells in the internal shock model are small can also produce XRF-like events (Mochkovitch et al. 2003).

It has been proposed that XRFs are due to universal GRB jets in which the luminosity falls off like a power law from the jet axis (Zhang & Mészáros 2002; Rossi et al. 2002) and are viewed well off the jet axis (Zhang et al. 2004). However, Lamb, Donaghy & Graziani (2004) have shown that such a model predicts far more XRFs than GRBs, in conflict with the HETE-2 results described in this paper. A universal GRB jet model in which the luminosity falls off like a Gaussian may do better (Zhang et al. 2004).

Lamb, Donaghy & Graziani (2004) have shown that a unified description of XRFs, XRRs, and GRBs is possible in a model in which the GRB jet opening angle varies over a wide range. In this model, XRFs are due to jets with wide opening angles while GRBs are due to jets with narrow opening angles.

As this discussion suggests, understanding the properties of XRFs and XRRs, and clarifying the relationship between these two kinds of events and GRBs, could provide a deeper understanding of the prompt emission of GRBs. And as Lamb, Donaghy & Graziani (2004) have emphasized, XRFs may provide unique insights into the nature of GRB jets, the rate of GRBs, and the relationship between GRBs and Type Ic supernovae.

9. Conclusions

We have studied the global properties of 45 GRBs observed by HETE-2 during the first three years of its mission, focusing on the properties of XRFs and XRRs. We find that the numbers of XRFs, XRRs, and GRBs are comparable. We find that the durations and

the sky distributions of XRFs and XRRs are similar to those of GRBs. We also find that the spectral properties of XRFs and XRRs are similar to those of GRBs, except that the values of the peak energy $E_{\text{peak}}^{\text{obs}}$ of the burst spectrum in νF_{ν} , the peak flux F_{peak} , and the fluence S_E of XRFs are much smaller – and those of XRRs are smaller – than those of GRBs. Finally, we find that the distributions of all three kinds of bursts form a continuum in the $[S(2-30 \text{ keV}), S(30-400 \text{ keV})]$ -plane, the $[S(2-400 \text{ keV}), E_{\text{peak}}]$ -plane, and the $[F_{\text{peak}}(50-300 \text{ keV}), E_{\text{peak}}^{\text{obs}}]$ -plane. These results provide strong evidence that all three kinds of bursts arise from the same phenomenon. They also provide constraints on theoretical models of XRFs.

We would like to thank Dr. R. Marc Kippen for providing us the WFC/BATSE spectral parameters. The *HETE* mission is supported in the U.S. by NASA contract NASW-4690; in Japan, in part by the Ministry of Education, Culture, Sports, Science, and Technology Grant-in-Aid 12440063; and in France, by CNES contract 793-01-8479. K. Hurley is grateful for *Ulysses* support under contract JPL 958059 and for *HETE* support under contract MIT-SC-R-293291. G. Pizzichini acknowledges support by the Italian Space Agency.

REFERENCES

- Amati, L., et al. 2002, *A&A*, 390, 81
- Atteia, J-L, et al. 2003, in *Gamma-Ray Bursts and Afterglow Astronomy*, eds. G. R. Ricker and R. Vanderspek (New York: AIP), 17
- Band, D. L., et al. 1993, *ApJ*, 413, 281
- Barraud, C., et al. 2003, *A&A*, 400, 1021
- Bloom, J. S., et al. 2003, *ApJ*, 599, 957
- Dermer, C. D., Chiang, J., and Böttcher 1999, *ApJ*, 513, 656
- Dermer, C. D., and Mitman, K. E. 2003, in *proc. of Third Rome Workshop: Gamma-Ray Bursts in the Afterglow Era* (astro-ph/0301340)
- Fynbo, J. P. U., et al. 2004, *ApJ*, 609, 962
- Heise, J., in't Zand, J., Kippen, R. M., & Woods, P. M., in *Proc. 2nd Rome Workshop: Gamma-Ray Bursts in the Afterglow Era*, eds. E. Costa, F. Frontera, J. Hjorth (Berlin: Springer-Verlag), 16

- Huang, Y. F., Dai, Z. G., and Lu, T. 2002, *MNRAS*, 332, 735
- Kawai, N., et al. 2003, in *Gamma-Ray Bursts and Afterglow Astronomy*, eds. G. R. Ricker and R. Vanderspek (New York: AIP), 25
- Kippen, R. M., Woods, P. M., Heise, J., in't Zand, J., Briggs, M. S., & Preece, R. D. 2002, in *Gamma-Ray Bursts and Afterglow Astronomy*, eds. G. R. Ricker and R. Vanderspek (New York: AIP), 244
- Lamb, D. Q., Donaghy, T. Q., and Graziani, C. 2004, submitted to *ApJ*(astro-ph/0312634)
- Lamb, D. Q., et al. 2004a, submitted to *ApJ*, (astro-ph/0206151)
- Lamb, D. Q., et al. 2004b, in preparation
- Mallozzi, R. S., Paciesas, W. S., Pendleton, G. N., Briggs, M. S., Preece, R. D., Meegan, C. A. & Fishman, G. J. 1995, *ApJ*, 454, 597
- Mészáros, P., Ramirez-Ruiz, E., Rees, M. J., & Zhang, B. 2002, *ApJ*, 578, 812
- Mochkovitch, R., Daigne, F., Barraud, C., & Atteia, J. L. 2003, *ASP Conference Series* (San Francisco: ASP), in press (astro-ph/0303289)
- Olive, J.-F., et al. 2003, in *Gamma-Ray Bursts and Astronomy*, eds. G. R. Ricker and R. Vanderspek (New York: AIP), 88
- Paciesas, W. S., et al. 1999, *ApJS*, 122, 465
- Preece, R. D., Briggs, M. S., Mallozzi, R. S., Pendleton, G. N., & Paciesas, W. S. 2000, *ApJS*, 126, 19
- Rossi, E., Lazzati, D., and Rees, M. J. 2002, *MNRAS*, 332, 945
- Sakamoto, T., et al. 2004, *ApJ*, 602, 875
- Sakamoto, T., et al. 2004, in preparation.
- Shirasaki, Y., et al. 2003b, *PASJ*, 55, 1033
- Soderberg, A. M., et al. 2004, *ApJ*, 606, 994
- Vanderspek, R., et al. 2004, in preparation
- Woosley, S. E., Zhang, W. & Heger, A. 2003, *ApJ*, submitted (astro-ph/0206004)

Yamazaki, R., Ioka K. & Nakamura T. 2002, ApJ, 571, L31

Yamazaki, R., Ioka K. & Nakamura T. 2003, ApJ, submitted (astro-ph/0212557)

Zhang, B. & Mészáros, P. 2002, ApJ, 571, 876

Zhang, B., Dai, X., Lloyd-Ronning, N. M., & Mészáros, P. 2004, 601, L119

Table 1. Some Properties of 45 HETE-2 GRBs

GRB	BID	θ_X	θ_Y	TT ^a	TS ^b	EB ^c	R.A.	Dec.	l	b	error ^d	t_{50} (WXM)	t_{90} (WXM)
GRB010213	10805	-2.41	13.60	—	—	—	10h31m36s	+05d30m39s	239.6	50.3	30.2'	8.6 ± 1.2	24.5 ± 1.2
GRB010225 ^e	1491	-23.10	0.97	G	1.3s	5-120	—	—	—	—	—	6.2 ± 1.3	15.9 ± 3.9
GRB010326B	1496	7.97	-15.02	G	160ms	5-120	11h24m24s	-11d09m57s	271.2	46.3	36'	1.7 ± 0.2	5.2 ± 0.2
GRB010612	1546	13.81	1.17	G	160ms	30-400	18h03m18s	-32d08m01s	359.2	-4.9	36'	17.4 ± 0.8	28.5 ± 0.2
GRB010613	1547	-30.50	25.17	G	1.3s	30-400	17h00m40s	+14d16m05s	33.9	30.9	36'	23.8 ± 1.2	51.8 ± 0.7
GRB010629B	1573	-26.60	8.29	G	1.3s	5-120	16h32m38s	-18d43m24s	358.6	19.5	15'	9.3 ± 0.3	16.2 ± 0.2
GRB010921	1761	-23.95	39.45	G	1.3s	5-120	23h01m53s	+44d16m12s	103.1	-14.3	20° × 15'	—	—
GRB010928	1770	-2.99	35.00	G	1.3s	30-400	23h28m55s	+30d39m11s	102.9	-26.7	16.4' × 11°	29.5 ± 3.5	59.0 ± 1.8
GRB011019	10823	-18.29	-17.63	—	—	—	00h42m50s	-12d26m58s	114.7	-75.2	35'	12.2 ± 1.3	31.6 ± 1.2
GRB011103	1829	-0.32	-10.94	XG	5.12s	—	03h20m37s	17d40m01s	166.1	-32.4	—	8.6 ± 1.7	19.7 ± 1.2
GRB011130	1864	-13.03	22.83	XG	5.12s	—	03h05m36s	+03d48m36s	174.4	-45.2	10'	23.8 ± 0.6	39.5 ± 0.4
GRB011212	10827	-1.60	9.71	—	—	—	05h00m05s	+32d07m39s	171.8	-6.3	11'	33.2 ± 1.2	72.5 ± 2.8
GRB020124	1896	14.65	-31.57	G	1.3s	30-400	09h32m49s	-11d27m35s	244.9	28.3	12'	18.6 ± 1.1	50.2 ± 2.3
GRB020127	1902	-7.51	20.76	G	5.12s	30-400	08h15m06s	+36d44m31s	184.7	31.8	8'	6.0 ± 0.3	17.6 ± 1.9
GRB020317	1959	-17.14	15.15	G	1.3s	5-120	10h23m21s	+12d44m38s	228.1	52.5	18'	2.4 ± 0.4	14.7 ± 0.5
GRB020331	1963	6.91	-14.33	G	160ms	30-400	13h16m34s	-17d52m29s	311.3	44.6	10'	35.7 ± 1.8	78.7 ± 1.8
GRB020531	2042	22.94	11.33	G	20ms	30-400	15h14m45s	-19d21m35s	343.6	32.0	38'	1.1 ± 0.2	2.5 ± 0.3
GRB020625	2081	5.64	10.12	G	5.2s	30-400	20h44m14s	+07d10m12s	53.3	-21.1	13.8'	13.5 ± 1.2	119.2 ± 2.4
GRB020801	2177	4.73	35.44	G	1.3s	30-400	21h02m14s	-53d46m13s	343.9	-40.7	13.9'	262.9 ± 4.2	348.9 ± 4.4
GRB020812	2257	-15.30	-12.13	G	1.3s	30-400	20h38m48s	-05d23m34s	40.7	-26.3	13.8'	14.1 ± 0.6	42.0 ± 1.0
GRB020813	2262	0.04	-3.81	G	1.3s	30-400	19h46m38s	-19d35m16s	20.8	-20.7	1'(S)	>30.0	>89.0
GRB020819	2275	17.70	-22.45	G	160ms	30-400	23h27m07s	+06d21m50s	88.5	-50.8	7'	11.5 ± 0.3	46.9 ± 2.0
GRB020903	2314	4.20	12.64	XG	5.12s	—	22h49m25s	-20d53m59s	38.9	-61.5	16.7'	4.8 ± 0.4	10.0 ± 0.7
GRB021004	2380	3.92	-12.39	G	5.2s	30-400	00h26m57s	+18d55m44s	114.9	-43.6	2'(S)	26.6 ± 1.0	77.1 ± 2.6
GRB021021	10623	15.24	11.92	—	—	—	00h17m23s	-01d37m00s	103.8	-63.2	20'	22.1 ± 1.2	56.5 ± 1.2
GRB021104	2434	22.56	22.38	G	1.3s	5-120	03h53m48s	+37d57m12s	158.1	-12.2	26'	10.2 ± 0.5	18.1 ± 0.2
GRB021112	2448	12.24	27.06	G	1.3s	5-120	02h36m52s	+48d50m56s	140.2	-10.5	20'	6.8 ± 1.2	14.7 ± 1.1
GRB021211	2493	-12.55	-0.01	G	160ms	30-400	08h09m00s	+06d44m20s	215.7	20.3	2'(S)	3.1 ± 0.1	13.3 ± 0.3
GRB030115	2533	13.01	-3.11	G	1.3s	30-400	11h18m30s	+15d02m17s	237.4	65.2	2'(S)	9.2 ± 0.5	49.6 ± 4.3
GRB030226	10893	-13.00	-16.27	—	—	—	11h33m01s	+25d53m56s	212.5	72.4	2'(S)	66.4 ± 3.9	137.7 ± 4.9
GRB030323	2640	4.05	35.06	XG	320ms	—	11h06m54s	-21d51m00s	273.0	34.9	18'	13.9 ± 1.6	32.6 ± 2.7
GRB030324	2641	-26.35	0.57	G	1.3s	30-400	13h37m11s	-00d19m22s	326.6	60.4	7'	8.9 ± 0.3	25.8 ± 0.8
GRB030328	2650	5.05	7.14	G	1.3s	5-120	12h10m51s	-09d21m05s	286.4	52.2	1'(S)	106.9 ± 1.2	315.8 ± 3.0
GRB030329	2652	26.68	-29.00	G	1.3s	5-120	10h44m49s	+21d28m44s	217.1	60.7	2'(S)	12.1 ± 0.2	33.1 ± 0.5
GRB030416	10897	-1.98	-11.32	—	—	—	11h06m51s	-02d52m58s	258.8	50.8	7'	19.7 ± 1.7	61.5 ± 1.2

Table 1—Continued

GRB	BID	θ_X	θ_Y	TT ^a	TS ^b	EB ^c	R.A.	Dec.	l	b	error ^d	t ₅₀ (WXM)	t ₉₀ (WXM)
GRB030418	2686	7.45	-9.66	XG	13.280s	—	10h54m53s	-06d59m22s	259.1	45.7	9'	38.7 ± 0.9	117.6 ± 0.7

Table 1—Continued

GRB	BID	θ_X	θ_Y	TT ^a	TS ^b	EB ^c	R.A.	Dec.	l	b	error ^d	t ₅₀ (WXM)	t ₉₀ (WXM)
GRB030429	2695	8.88	11.83	XG	6.72s	—	12h13m06s	-20d56m00s	291.0	41.1	1'(S)	38.4 ± 1.5	77.4 ± 1.2
GRB030519	2716	-41.00	16.18	G	160ms	30-400	14h58m18s	-32d56m57s	331.5	22.8	30'	6.1 ± 0.6	13.8 ± 0.7
GRB030528	2724	20.66	6.14	G	1.3s	30-400	17h04m02s	-22d38m59s	0.0	11.3	2'(S)	20.8 ± 1.2	49.2 ± 1.2
GRB030723	2777	1.55	10.93	XG	6.72s	WXM	21h49m30s	-27d42m06s	21.2	-49.9	2'(S)	9.9 ± 0.3	20.2 ± 0.5
GRB030725	2779	18.41	33.10	G	160ms	5-120	20h33m47s	-50d45m49s	348.2	-36.6	14.4'	68.3 ± 3.4	200.0 ± 2.5
GRB030821	2814	12.13	32.47	G	1.3s	30-400	21h42m33s	-45d12m12s	354.3	-48.5	120'x10'	11.7 ± 1.5	22.9 ± 0.5
GRB030823	2818	11.67	-32.65	G	5.2s	5-120	21h30m47s	+21d59m46s	73.2	-21.0	5.4'	30.2 ± 1.4	66.4 ± 1.9
GRB030824	2821	-29.79	-31.43	G	1.3s	5-120	00h05m02s	+19d55m37s	108.3	-41.6	11.2'	13.1 ± 1.8	36.4 ± 0.4
GRB030913	2849	-2.05	4.62	G	1.3s	30-400	20h58m02s	-02d12m32s	46.5	-29.0	30'	2.9 ± 0.3	6.7 ± 0.3

^aTriggered type; G: FREGATE triggered, XG: FREGATE triggered by XDSP.

^bTrigger time-scale.

^cTrigger energy band in keV.

^dLocation error radius (90% confidence). “S” indicates localization by the SXC.

^eSince the attitude control camera was not operational, the celestial coordinates is not available.

Table 2: Spectral Parameters of 45 HETE-2 GRBs

GRB	Class ^a	Model ^b	α	β	E_{peak} [keV]	K_{15}^c	χ^2_{ν}	D.O.F.
GRB010213	XRF	Band	-1.00(fixed)	$-2.96^{+0.22}_{-0.54}$	$3.41^{+0.35}_{-0.40}$	$44.63^{+7.63}_{-5.19}$	0.940	44
GRB010225	XRF	PLE	$-1.31^{+0.30}_{-0.26}$	—	$31.57^{+26.50}_{-9.17}$	$6.75^{+2.93}_{-1.87}$	0.925	39
GRB010326B [†]	XRR	PLE	$-1.08^{+0.25}_{-0.22}$	—	$51.77^{+18.61}_{-11.25}$	$13.19^{+3.07}_{-2.31}$	0.856	111
GRB010612	GRB	PLE	$-1.07^{+0.19}_{-0.17}$	—	$244.50^{+285.07}_{-81.97}$	$2.93^{+0.37}_{-0.36}$	0.884	65
GRB010613	XRR	Band	$-0.95^{+0.33}_{-0.26}$	$-2.01^{+0.09}_{-0.15}$	$46.25^{+17.78}_{-10.38}$	$15.24^{+4.37}_{-2.43}$	0.785	134
GRB010629B	XRR	PLE	$-1.12^{+0.14}_{-0.13}$	—	$45.57^{+4.61}_{-3.84}$	$20.05^{+1.77}_{-1.56}$	0.817	110
GRB010921 [†]	XRR	PLE	$-1.55^{+0.08}_{-0.07}$	—	$88.63^{+21.76}_{-13.79}$	$41.79^{+1.75}_{-1.63}$	0.939	140
GRB010928 [†]	GRB	PLE	$-0.66^{+0.10}_{-0.09}$	—	$409.50^{+118.46}_{-74.98}$	$6.30^{+0.55}_{-0.52}$	0.825	125
GRB011019	XRF	PLE	-1.43 (fixed)	—	$18.71^{+18.33}_{-8.72}$	$2.46^{+0.82}_{-0.63}$	0.854	68
GRB011103	XRR	PL	$-1.73^{+0.24}_{-0.29}$	—	—	$2.72^{+0.83}_{-0.88}$	1.266	38
GRB011130	XRF	PL	—	$-2.65^{+0.26}_{-0.33}$	< 3.9 ^d	$0.69^{+0.29}_{-0.26}$	1.016	40
GRB011212	XRF	PL	—	$-2.07^{+0.19}_{-0.22}$	—	$0.72^{+0.17}_{-0.18}$	0.795	54
GRB020124	XRR	PLE	$-0.79^{+0.15}_{-0.14}$	—	$86.93^{+18.11}_{-12.45}$	$9.24^{+0.98}_{-0.88}$	0.710	95
GRB020127	XRR	PLE	$-1.03^{+0.14}_{-0.13}$	—	$104.00^{+47.00}_{-11.12}$	$4.50^{+0.58}_{-0.51}$	0.746	110
GRB020317	XRF	PLE	$-0.61^{+0.61}_{-0.52}$	—	$28.41^{+12.68}_{-7.41}$	$7.27^{+7.73}_{-3.12}$	0.923	53
GRB020331	GRB	PLE	$-0.79^{+0.13}_{-0.12}$	—	$91.57^{+20.99}_{-14.09}$	$4.03^{+0.46}_{-0.41}$	0.732	111
GRB020531	GRB	PLE	$-0.83^{+0.14}_{-0.13}$	—	$230.60^{+113.10}_{-58.11}$	$20.99^{+2.31}_{-2.21}$	0.831	141
GRB020625	XRF	PLE	-1.14 (fixed)	—	$8.52^{+5.44}_{-2.91}$	$2.84^{+1.05}_{-0.78}$	0.781	55
GRB020801 [†]	GRB	Band	$-0.32^{+0.44}_{-0.34}$	$-2.01^{+0.17}_{-0.25}$	$53.35^{+14.37}_{-11.12}$	$5.66^{+1.92}_{-1.02}$	0.638	140
GRB020812	XRR	PLE	$-1.09^{+0.29}_{-0.25}$	—	$87.62^{+106.03}_{-29.57}$	$2.27^{+0.61}_{-0.47}$	0.664	68
GRB020813 [†]	GRB	Band	$-0.94^{+0.03}_{-0.03}$	$-1.57^{+0.03}_{-0.04}$	$142.10^{+14.05}_{-12.91}$	$20.74^{+0.51}_{-0.47}$	1.160	140
GRB020819	XRR	Band	$-0.90^{+0.17}_{-0.14}$	$-1.99^{+0.18}_{-0.48}$	$49.90^{+17.88}_{-12.19}$	$10.71^{+2.47}_{-1.65}$	0.945	108
GRB020903	XRF	PL	—	$-2.62^{+0.42}_{-0.55}$	< 5.0 ^d (2.6 ^{+1.4} _{-0.8})	$0.41^{+0.34}_{-0.25}$	0.845	26
GRB021004	XRR	PLE	$-1.01^{+0.19}_{-0.17}$	—	$79.79^{+53.35}_{-22.97}$	$2.77^{+0.60}_{-0.48}$	0.949	68
GRB021021	XRF	PLE	-1.33 (fixed)	—	$15.38^{+14.24}_{-7.47}$	$1.24^{+0.50}_{-0.37}$	0.879	41
GRB021104 [†]	XRF	PLE	$-1.11^{+0.54}_{-0.46}$	—	$28.21^{+17.41}_{-7.88}$	$7.59^{+5.31}_{-2.55}$	0.744	38
GRB021112	XRR	PLE	$-0.94^{+0.42}_{-0.32}$	—	$57.15^{+38.90}_{-20.70}$	$6.57^{+3.47}_{-1.83}$	1.126	61
GRB021211	XRR	Band	$-0.86^{+0.10}_{-0.09}$	$-2.18^{+0.14}_{-0.25}$	$45.56^{+7.84}_{-6.23}$	$32.58^{+4.16}_{-3.32}$	1.149	140
GRB030115	XRR	PLE	$-1.28^{+0.14}_{-0.13}$	—	$82.79^{+52.82}_{-22.26}$	$3.50^{+0.53}_{-0.46}$	0.812	67
GRB030226	GRB	PLE	$-0.89^{+0.17}_{-0.15}$	—	$97.12^{+26.98}_{-17.06}$	$3.47^{+0.42}_{-0.38}$	0.894	139
GRB030323	XRR	PL	$-1.62^{+0.24}_{-0.25}$	—	—	$2.19^{+0.64}_{-0.67}$	0.835	33
GRB030324	XRR	PLE	$-1.45^{+0.14}_{-0.12}$	—	$146.80^{+627.57}_{-65.49}$	$4.94^{+0.72}_{-0.60}$	0.882	76
GRB030328	GRB	Band	$-1.14^{+0.03}_{-0.03}$	$-2.09^{+0.19}_{-0.40}$	$126.30^{+13.89}_{-13.10}$	$6.64^{+0.20}_{-0.18}$	0.982	140
GRB030329	XRR	Band	$-1.26^{+0.01}_{-0.02}$	$-2.28^{+0.05}_{-0.06}$	$67.86^{+2.31}_{-2.15}$	$146.20^{+1.70}_{-1.70}$	1.537	139
GRB030416	XRF	PL	—	$-2.31^{+0.13}_{-0.15}$	< 3.8 ^d (2.6 ^{+0.5} _{-1.8})	$0.92^{+0.17}_{-0.17}$	0.870	54
GRB030418	XRR	PLE	$-1.46^{+0.14}_{-0.13}$	—	$46.10^{+31.96}_{-13.70}$	$2.43^{+0.48}_{-0.37}$	0.929	68
GRB030429	XRF	PLE	$-1.12^{+0.25}_{-0.22}$	—	$35.04^{+11.75}_{-7.90}$	$4.05^{+1.32}_{-0.90}$	0.720	68
GRB030519 [†]	GRB	Band	$-0.75^{+0.07}_{-0.06}$	$-1.72^{+0.05}_{-0.07}$	$137.60^{+17.80}_{-15.36}$	$73.21^{+2.06}_{-1.90}$	0.742	124
GRB030528 [†]	XRF	Band	$-1.33^{+0.15}_{-0.12}$	$-2.65^{+0.29}_{-0.98}$	$31.84^{+4.67}_{-4.97}$	$13.94^{+2.44}_{-1.48}$	0.809	109
GRB030723	XRF	PL	—	$-1.90^{+0.16}_{-0.20}$	< 8.9 ^d	$1.00^{+0.21}_{-0.22}$	0.952	142
GRB030725	XRR	PLE	$-1.51^{+0.04}_{-0.04}$	—	$102.80^{+19.05}_{-13.73}$	$15.71^{+0.54}_{-0.50}$	1.069	141
GRB030821	XRR	PLE	$-0.88^{+0.13}_{-0.12}$	—	$84.26^{+15.12}_{-10.88}$	$8.74^{+0.77}_{-0.70}$	0.971	98
GRB030823	XRF	PLE	$-1.31^{+0.20}_{-0.18}$	—	$26.57^{+7.45}_{-5.02}$	$8.26^{+2.34}_{-1.59}$	0.708	110
GRB030824	XRF	PL	—	$-2.14^{+0.13}_{-0.14}$	< 8.7 ^d (6.1 ^{+1.9} _{-4.2})	$5.25^{+0.76}_{-0.78}$	0.813	53
GRB030913	GRB	PLE	$-0.82^{+0.28}_{-0.24}$	—	$119.70^{+113.25}_{-36.47}$	$3.53^{+0.75}_{-0.62}$	0.740	53

a GRB classification; XRF: X-ray-flash, XRR: X-ray-rich GRB, GRB: GRB
b Spectral model; PL: Power-law; PLE: Power-law times exponential cutoff; Band: Band function
c Normalization at 15 keV in units of 10^{-2} photons $\text{cm}^{-2} \text{s}^{-1} \text{keV}^{-1}$
d 99.7% upper limit and 90% confidence interval (in parenthesis) derived by the *constrained* Band function
[†] The constant factor is multiplied to the spectral model.

Table 3: Photon Number and Photon Energy Fluences of 45 HETE-2 GRBs

GRB	Duration [sec.]	Photon fluence ^a			Energy fluence ^b			X/γ ratio
		2-30 keV	30-400 keV	2-400 keV	2-30 keV	30-400 keV	2-400 keV	
GRB010213	34.41	111.10 ^{+5.20} _{-4.80}	0.69 ^{+0.69} _{-0.34}	111.80 ^{+5.50} _{-4.80}	7.88 ^{+0.25} _{-0.54}	0.69 ^{+0.58} _{-0.32}	8.58 ^{+1.01} _{-0.94}	11.38
GRB010225	9.76	28.30 ^{+3.71} _{-3.80}	2.73 ^{+0.98} _{-0.88}	31.04 ^{+3.90} _{-3.91}	3.48 ^{+0.36} _{-0.36}	2.40 ^{+1.72} _{-0.94}	5.89 ^{+1.69} _{-1.06}	1.45
GRB010326B	3.50	16.77 ^{+2.83} _{-2.77}	3.25 ^{+0.52} _{-0.56}	19.98 ^{+2.91} _{-2.76}	2.40 ^{+0.27} _{-0.27}	3.22 ^{+0.92} _{-0.76}	5.62 ^{+0.95} _{-0.81}	0.75
GRB010612	47.19	56.63 ^{+13.21} _{-11.80}	29.26 ^{+2.36} _{-1.89}	85.89 ^{+13.68} _{-12.27}	8.84 ^{+1.35} _{-1.31}	50.23 ^{+7.12} _{-6.21}	59.05 ^{+6.37} _{-6.53}	0.18
GRB010613	141.56	672.40 ^{+11.80} _{-90.60}	168.50 ^{+5.60} _{-5.70}	840.90 ^{+11.80} _{-92.00}	101.50 ^{+6.60} _{-6.54}	227.60 ^{+12.60} _{-12.50}	329.40 ^{+13.70} _{-13.80}	0.45
GRB010629B	24.58	182.90 ^{+21.40} _{-20.20}	29.99 ^{+1.72} _{-1.72}	212.90 ^{+21.30} _{-20.20}	25.41 ^{+1.67} _{-1.66}	28.56 ^{+2.69} _{-2.47}	53.97 ^{+3.32} _{-3.13}	0.89
GRB010921	23.85	610.10 ^{+48.90} _{-45.80}	88.48 ^{+3.58} _{-3.57}	698.80 ^{+48.20} _{-45.50}	71.60 ^{+3.42} _{-3.20}	112.60 ^{+8.60} _{-8.40}	184.20 ^{+9.70} _{-9.50}	0.64
GRB010928	34.55	70.48 ^{+9.68} _{-8.98}	104.70 ^{+3.10} _{-3.10}	174.80 ^{+10.00} _{-9.30}	13.71 ^{+1.24} _{-1.35}	225.70 ^{+9.10} _{-9.50}	239.30 ^{+9.20} _{-4.80}	0.06
GRB011019	24.57	27.52 ^{+5.65} _{-5.65}	1.47 ^{+1.23} _{-0.98}	28.99 ^{+5.65} _{-5.65}	3.03 ^{+0.58} _{-0.58}	1.10 ^{+1.39} _{-0.74}	4.13 ^{+1.54} _{-1.14}	2.77
GRB011103	14.75	30.83 ^{+5.01} _{-5.02}	4.13 ^{+3.98} _{-2.21}	34.96 ^{+6.78} _{-6.35}	3.31 ^{+0.79} _{-0.71}	6.22 ^{+3.72} _{-2.84}	9.53 ^{+8.73} _{-4.30}	0.53
GRB011130	50.00	86.00 ^{+13.00} _{-13.00}	1.00 ^{+1.00} _{-0.50}	87.00 ^{+12.50} _{-13.00}	5.85 ^{+0.98} _{-0.96}	0.98 ^{+1.17} _{-0.62}	6.83 ^{+1.90} _{-1.46}	5.96
GRB011212	57.68	47.30 ^{+6.92} _{-6.92}	2.31 ^{+1.73} _{-0.58}	49.60 ^{+7.50} _{-6.92}	4.24 ^{+0.64} _{-0.64}	3.37 ^{+2.53} _{-1.68}	7.61 ^{+2.90} _{-2.16}	1.26
GRB020124	40.63	115.00 ^{+11.80} _{-11.80}	51.19 ^{+3.66} _{-4.06}	165.80 ^{+13.00} _{-12.20}	19.74 ^{+1.40} _{-1.41}	61.33 ^{+8.79} _{-7.63}	81.04 ^{+8.86} _{-7.70}	0.32
GRB020127	25.63	43.57 ^{+4.10} _{-4.10}	15.63 ^{+1.80} _{-1.53}	59.21 ^{+4.61} _{-4.62}	6.73 ^{+0.51} _{-0.50}	20.49 ^{+4.48} _{-3.65}	27.22 ^{+4.43} _{-3.63}	0.33
GRB020317	10.00	13.80 ^{+3.50} _{-3.30}	1.70 ^{+0.80} _{-0.70}	15.50 ^{+3.70} _{-3.40}	2.16 ^{+0.37} _{-0.38}	1.29 ^{+0.88} _{-0.64}	3.45 ^{+0.94} _{-0.79}	1.68
GRB020331	75.00	93.00 ^{+7.50} _{-6.75}	43.50 ^{+3.75} _{-3.75}	136.50 ^{+8.30} _{-8.30}	16.07 ^{+1.04} _{-1.03}	53.32 ^{+8.52} _{-7.39}	69.40 ^{+8.45} _{-7.45}	0.30
GRB020531	1.04	7.54 ^{+1.12} _{-1.09}	6.18 ^{+0.48} _{-0.48}	13.72 ^{+1.22} _{-1.21}	1.33 ^{+0.14} _{-0.14}	10.96 ^{+1.35} _{-1.34}	12.30 ^{+1.35} _{-1.35}	0.12
GRB020625	41.94	24.74 ^{+4.20} _{-3.77}	0.19 ^{+0.51} _{-0.18}	25.16 ^{+3.78} _{-3.77}	2.37 ^{+0.55} _{-0.50}	0.12 ^{+0.35} _{-0.11}	2.49 ^{+0.83} _{-0.58}	20.49
GRB020801	117.97	130.90 ^{+27.20} _{-23.50}	69.60 ^{+4.72} _{-4.72}	200.50 ^{+27.20} _{-23.50}	25.66 ^{+2.83} _{-2.72}	95.23 ^{+10.67} _{-10.54}	121.00 ^{+11.00} _{-10.90}	0.27
GRB020812	60.16	52.94 ^{+9.62} _{-9.62}	15.64 ^{+3.01} _{-3.01}	68.58 ^{+9.83} _{-9.62}	7.91 ^{+1.09} _{-1.09}	19.15 ^{+8.18} _{-8.86}	27.06 ^{+5.98} _{-5.98}	0.41
GRB020813	113.00	845.20 ^{+22.60} _{-21.40}	480.20 ^{+4.60} _{-4.50}	1325.00 ^{+24.00} _{-22.00}	138.50 ^{+2.70} _{-2.30}	839.60 ^{+12.30} _{-12.50}	978.70 ^{+12.70} _{-12.80}	0.16
GRB020819	50.16	163.00 ^{+8.50} _{-9.00}	45.65 ^{+3.51} _{-3.01}	208.70 ^{+9.50} _{-9.60}	25.20 ^{+1.10} _{-1.11}	62.53 ^{+8.33} _{-9.27}	87.80 ^{+8.39} _{-9.47}	0.40
GRB020903	13.00	12.61 ^{+2.73} _{-2.60}	0.16 ^{+0.34} _{-0.13}	12.74 ^{+2.73} _{-2.73}	0.83 ^{+0.28} _{-0.24}	0.16 ^{+0.44} _{-0.14}	0.95 ^{+0.62} _{-0.33}	7.31
GRB021004	49.70	49.70 ^{+4.97} _{-4.47}	15.41 ^{+2.48} _{-2.98}	65.11 ^{+5.46} _{-5.47}	7.65 ^{+0.69} _{-0.69}	17.79 ^{+7.01} _{-5.00}	25.45 ^{+6.85} _{-5.04}	0.43
GRB021021	49.15	23.10 ^{+5.41} _{-5.41}	0.88 ^{+1.15} _{-0.69}	24.08 ^{+5.41} _{-5.89}	2.51 ^{+1.03} _{-1.09}	0.62 ^{+1.18} _{-0.49}	3.13 ^{+1.39} _{-1.06}	4.03
GRB021104	31.41	78.84 ^{+29.86} _{-21.05}	7.54 ^{+3.14} _{-2.51}	86.38 ^{+30.12} _{-21.36}	10.32 ^{+2.06} _{-1.80}	6.13 ^{+4.40} _{-2.67}	16.38 ^{+5.00} _{-3.34}	1.69
GRB021112	4.00	8.48 ^{+2.08} _{-2.00}	2.12 ^{+0.64} _{-0.64}	10.60 ^{+2.20} _{-2.12}	1.31 ^{+0.25} _{-0.25}	2.14 ^{+1.08} _{-0.90}	3.45 ^{+1.09} _{-0.93}	0.61
GRB021211	8.00	74.56 ^{+2.40} _{-2.40}	18.88 ^{+0.88} _{-0.88}	93.44 ^{+2.64} _{-2.56}	11.60 ^{+0.29} _{-0.29}	23.71 ^{+2.03} _{-2.01}	35.34 ^{+2.07} _{-2.06}	0.49
GRB030115	36.00	58.68 ^{+5.40} _{-5.40}	12.60 ^{+1.44} _{-1.80}	71.28 ^{+5.76} _{-5.76}	7.89 ^{+0.61} _{-0.61}	15.17 ^{+4.02} _{-3.20}	23.05 ^{+3.98} _{-3.23}	0.52
GRB030226	68.81	79.82 ^{+10.32} _{-10.32}	33.72 ^{+3.44} _{-3.44}	114.20 ^{+10.30} _{-11.76}	13.20 ^{+1.18} _{-1.18}	42.92 ^{+6.85} _{-6.02}	56.12 ^{+6.93} _{-6.14}	0.31
GRB030323	19.61	29.22 ^{+16.08} _{-12.55}	5.49 ^{+1.57} _{-1.76}	34.71 ^{+15.49} _{-12.55}	3.40 ^{+1.29} _{-1.21}	8.91 ^{+3.84} _{-3.48}	12.30 ^{+3.68} _{-3.43}	0.38
GRB030324	15.73	43.73 ^{+4.56} _{-4.25}	8.97 ^{+1.25} _{-1.26}	52.70 ^{+4.71} _{-4.57}	5.49 ^{+0.44} _{-0.44}	12.75 ^{+3.35} _{-3.01}	18.23 ^{+3.34} _{-3.01}	0.43
GRB030328	199.23	555.90 ^{+11.90} _{-10.00}	193.30 ^{+5.90} _{-4.00}	751.10 ^{+12.00} _{-12.00}	81.86 ^{+1.31} _{-1.29}	287.40 ^{+13.90} _{-14.10}	369.50 ^{+14.00} _{-14.20}	0.28
GRB030329	62.94	4121.00 ^{+41.00} _{-42.00}	843.40 ^{+5.70} _{-5.70}	4963.00 ^{+43.00} _{-40.00}	553.10 ^{+3.10} _{-3.20}	1076.00 ^{+13.00} _{-14.00}	1630.00 ^{+14.00} _{-13.00}	0.51
GRB030416	78.64	114.00 ^{+9.50} _{-10.20}	3.15 ^{+1.57} _{-0.79}	117.20 ^{+10.20} _{-10.20}	8.98 ^{+0.87} _{-0.87}	3.72 ^{+1.85} _{-1.38}	12.70 ^{+2.47} _{-2.09}	2.42
GRB030418	110.10	143.10 ^{+8.80} _{-8.80}	16.51 ^{+4.41} _{-3.30}	160.70 ^{+8.90} _{-9.90}	17.11 ^{+1.09} _{-1.10}	17.34 ^{+7.27} _{-5.22}	34.45 ^{+7.23} _{-5.48}	0.99
GRB030429	24.58	35.15 ^{+4.67} _{-4.43}	4.42 ^{+0.98} _{-1.23}	39.57 ^{+4.67} _{-4.67}	4.74 ^{+0.49} _{-0.49}	3.80 ^{+1.40} _{-1.17}	8.54 ^{+1.48} _{-1.32}	1.25
GRB030519	20.97	485.70 ^{+24.50} _{-23.90}	357.50 ^{+2.30} _{-4.40}	843.20 ^{+24.30} _{-23.50}	87.05 ^{+2.43} _{-2.38}	609.30 ^{+9.70} _{-9.70}	696.70 ^{+9.90} _{-9.90}	0.14
GRB030528	83.56	512.20 ^{+40.10} _{-39.30}	53.48 ^{+3.34} _{-3.34}	565.70 ^{+40.90} _{-38.40}	62.54 ^{+2.80} _{-2.79}	56.34 ^{+7.13} _{-7.32}	119.00 ^{+7.60} _{-7.80}	1.11
GRB030723	31.25	28.70 ^{+4.18} _{-4.15}	0.58 ^{+3.30} _{-0.49}	29.27 ^{+7.49} _{-4.49}	2.84 ^{+0.50} _{-0.50}	0.38 ^{+5.56} _{-0.33}	3.23 ^{+5.82} _{-0.76}	7.47
GRB030725	83.88	785.10 ^{+27.70} _{-27.70}	126.70 ^{+4.20} _{-4.20}	911.80 ^{+28.50} _{-27.70}	94.12 ^{+2.27} _{-2.25}	166.70 ^{+10.30} _{-10.10}	260.80 ^{+10.60} _{-10.40}	0.56
GRB030821	21.21	60.66 ^{+6.15} _{-5.73}	23.12 ^{+1.48} _{-1.49}	83.78 ^{+6.36} _{-5.94}	9.96 ^{+0.63} _{-0.64}	27.47 ^{+3.35} _{-2.99}	37.43 ^{+3.41} _{-3.07}	0.36
GRB030823	55.56	191.10 ^{+18.40} _{-17.20}	15.56 ^{+3.33} _{-3.34}	206.70 ^{+18.30} _{-18.40}	23.05 ^{+1.56} _{-1.55}	12.74 ^{+4.43} _{-3.53}	35.80 ^{+4.63} _{-3.97}	1.81
GRB030824	15.73	103.30 ^{+15.30} _{-15.05}	4.72 ^{+1.42} _{-1.42}	107.90 ^{+15.10} _{-14.78}	8.90 ^{+1.07} _{-1.07}	5.83 ^{+2.38} _{-1.89}	14.73 ^{+2.72} _{-2.42}	1.53
GRB030913	9.12	10.49 ^{+1.82} _{-1.83}	5.84 ^{+0.82} _{-0.82}	16.32 ^{+2.01} _{-2.09}	1.81 ^{+0.23} _{-0.23}	8.04 ^{+2.69} _{-1.93}	9.86 ^{+2.66} _{-1.73}	0.23

a Photon number fluences are in units of photon cm⁻²
 b Photon energy fluences are in units of 10⁻⁷ erg cm⁻²

Table 4: Peak (1 s) Photon Number Flux of 45 HETE-2 GRBs

GRB	Class ^a	Model ^b	$F_{\text{peak}(2-30 \text{ keV})}^N$ ^c	$F_{\text{peak}(30-400 \text{ keV})}^N$	$F_{\text{peak}(2-400 \text{ keV})}^N$	$F_{\text{peak}(50-300 \text{ keV})}^N$
GRB010213	XRF	Band	6.33 ± 0.77	$(2.97 \pm 0.55) \times 10^{-3}$	6.33 ± 0.81	$(1.08 \pm 0.15) \times 10^{-2}$
GRB010225	XRF	PLE	5.11 ± 2.36	0.33 ± 0.17	5.45 ± 2.39	$(9.56 \pm 9.37) \times 10^{-2}$
GRB010326B	XRR	PLE	10.52 ± 3.29	1.51 ± 0.35	12.03 ± 3.33	0.73 ± 0.24
GRB010612	GRB	PLE	4.32 ± 1.16	4.35 ± 0.48	8.67 ± 1.38	3.07 ± 0.35
GRB010613	XRR	Band	24.66 ± 11.60	2.68 ± 0.87	27.34 ± 11.19	1.23 ± 0.40
GRB010629B	XRR	PLE	39.08 ± 7.30	4.17 ± 0.42	43.25 ± 7.40	1.86 ± 0.26
GRB010921	XRR	PLE	34.20 ± 4.05	5.74 ± 0.46	39.93 ± 4.21	3.19 ± 0.30
GRB010928	GRB	PLE	3.83 ± 0.76	6.91 ± 0.45	10.74 ± 0.94	5.02 ± 0.46
GRB011019	XRF	PL	3.62 ± 1.41	0.15 ± 0.13	3.76 ± 1.44	$(7.41 \pm 7.33) \times 10^{-2}$
GRB011103	XRR	PL	4.42 ± 1.12	0.14 ± 0.08	4.55 ± 1.14	$(6.53 \pm 4.27) \times 10^{-2}$
GRB011130	XRF	PL	5.27 ± 1.27	$(8.20 \pm 6.28) \times 10^{-2}$	5.35 ± 1.28	$(3.57 \pm 3.21) \times 10^{-2}$
GRB011212	XRF	PL	1.13 ± 0.97	$< 7.66 \times 10^{-2}$	1.14 ± 0.96	$< 4.43 \times 10^{-2}$
GRB020124	XRR	PLE	6.90 ± 1.63	2.49 ± 0.40	9.38 ± 1.77	1.43 ± 0.28
GRB020127	XRR	PLE	5.95 ± 1.17	2.17 ± 0.42	8.12 ± 1.50	1.27 ± 0.27
GRB020317	XRF	PLE	4.63 ± 1.04	0.64 ± 0.25	5.26 ± 1.13	0.20 ± 0.14
GRB020331	GRB	PLE	1.93 ± 0.37	1.72 ± 0.23	3.65 ± 0.51	1.19 ± 0.17
GRB020531	GRB	PLE	17.41 ± 4.46	5.56 ± 0.74	22.97 ± 4.69	3.58 ± 0.51
GRB020625	XRF	PL	2.86 ± 0.97	0.31 ± 0.17	3.17 ± 1.07	0.18 ± 0.10
GRB020801	GRB	Band	6.36 ± 1.13	1.38 ± 0.25	7.73 ± 2.11	0.79 ± 0.18
GRB020812	XRR	PLE	2.48 ± 0.84	0.84 ± 0.26	3.32 ± 1.00	0.47 ± 0.17
GRB020813	GRB	Band	19.53 ± 1.29	12.79 ± 0.83	32.31 ± 2.07	8.31 ± 0.55
GRB020819	XRR	Band	12.09 ± 1.05	5.60 ± 0.44	17.68 ± 1.34	3.42 ± 0.29
GRB020903	XRF	PL	2.75 ± 0.66	$3.23_{-2.40}^{+6.73} \times 10^{-2}$	2.78 ± 0.67	$1.37_{-1.07}^{+3.68} \times 10^{-2}$
GRB021004	XRR	PLE	1.80 ± 0.38	0.89 ± 0.20	2.69 ± 0.50	0.43 ± 0.15
GRB021021	XRF	PL	2.14 ± 1.06	0.31 ± 0.24	2.45 ± 1.17	0.19 ± 0.16
GRB021104	XRF	PLE	4.23 ± 1.79	0.67 ± 0.22	4.89 ± 1.83	0.25 ± 0.13
GRB021112	XRR	PLE	3.45 ± 1.15	1.03 ± 0.37	4.47 ± 1.29	0.55 ± 0.28
GRB021211	XRR	Band	21.60 ± 1.33	8.36 ± 0.56	29.97 ± 1.74	4.10 ± 0.34
GRB030115	XRR	PLE	6.97 ± 1.32	1.16 ± 0.17	8.13 ± 1.38	1.16 ± 0.17
GRB030226	GRB	PLE	1.71 ± 0.51	0.99 ± 0.17	2.69 ± 0.57	0.63 ± 0.14
GRB030323	XRR	PL	3.37 ± 2.10	0.49 ± 0.22	3.86 ± 2.11	0.29 ± 0.15
GRB030324	XRR	PLE	6.63 ± 1.04	1.63 ± 0.30	8.27 ± 1.20	0.96 ± 0.23
GRB030328	GRB	Band	6.72 ± 0.51	4.92 ± 0.33	11.64 ± 0.85	3.32 ± 0.24
GRB030329	XRR	Band	378.59 ± 21.20	72.20 ± 3.77	450.88 ± 24.68	38.06 ± 2.04
GRB030416	XRF	PL	4.50 ± 0.91	0.26 ± 0.10	4.77 ± 0.94	$(1.39 \pm 0.62) \times 10^{-2}$
GRB030418	XRR	PLE	3.69 ± 0.85	0.30 ± 0.15	3.99 ± 0.91	0.13 ± 0.10
GRB030429	XRF	PLE	3.08 ± 0.72	0.71 ± 0.19	3.79 ± 0.79	0.29 ± 0.11
GRB030519	GRB	Band	7.52 ± 3.37	11.89 ± 4.81	19.41 ± 7.96	8.36 ± 3.38
GRB030528	XRF	Band	17.28 ± 1.52	0.61 ± 0.12	17.89 ± 1.57	$(1.50 \pm 0.55) \times 10^{-1}$
GRB030723	XRF	PLE	1.98 ± 0.38	$0.12_{-0.09}^{+0.14}$	2.10 ± 0.41	$3.06_{-2.57}^{+9.37} \times 10^{-2}$
GRB030725	XRR	PLE	24.83 ± 1.79	9.12 ± 0.55	33.96 ± 2.15	5.69 ± 0.37
GRB030821	XRR	PLE	3.84 ± 0.72	1.93 ± 0.27	5.77 ± 0.86	1.19 ± 0.19
GRB030823	XRF	PLE	7.03 ± 1.62	0.57 ± 0.26	7.60 ± 1.70	0.17 ± 0.14
GRB030824	XRF	PL	12.37 ± 3.77	0.28 ± 0.14	12.65 ± 3.82	$(1.29 \pm 0.74) \times 10^{-1}$
GRB030913	GRB	PLE	2.20 ± 0.48	1.36 ± 0.25	3.55 ± 0.63	0.89 ± 0.18

a GRB classification; XRF: X-ray-flash, XRR: X-ray-rich GRB, GRB: GRB

b Spectral model; PL: power-law, PLE: power-law times exponential cutoff, Band: Band function

c Photon number peak fluxes are in units of photons $\text{cm}^{-2}\text{s}^{-1}$

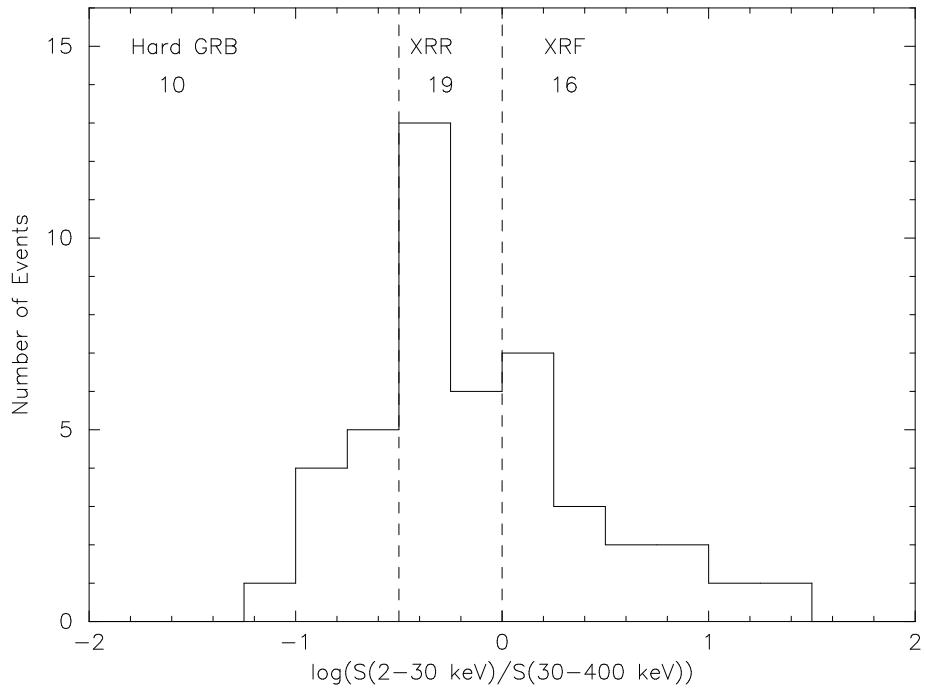


Fig. 1.— Distribution of the fluence ratio $S_E(2-30 \text{ keV})/S_E(30-400 \text{ keV})$. The dashed lines correspond to the borders between hard GRBs and XRRs, and between XRRs and XRFs.

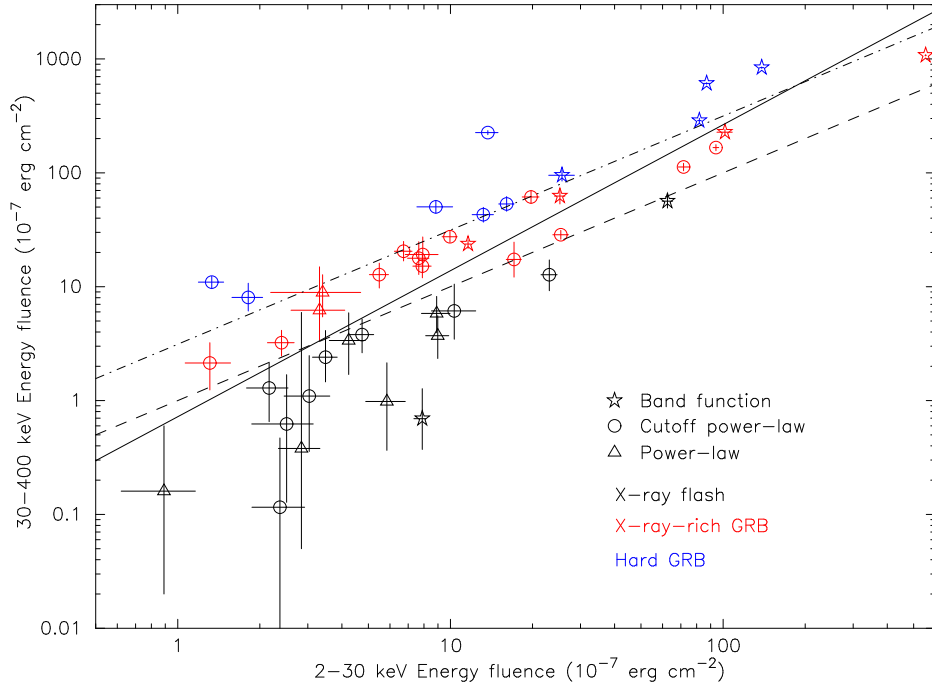


Fig. 2.— Distribution of the bursts in this study in the $[S_E(2-30 \text{ keV}), S_E(30-400 \text{ keV})]$ -plane. The dashed line corresponds to the boundary between XRFs and XRRs. The dash-dotted line corresponds to the boundary between XRRs and GRBs. The solid line is the best linear fit to the burst distribution, and is given by $S_E(30-400 \text{ keV}) = (0.722 \pm 0.161) \times S_E(2-30 \text{ keV})^{1.282 \pm 0.082}$. The correlation coefficient of the burst distribution is 0.851.

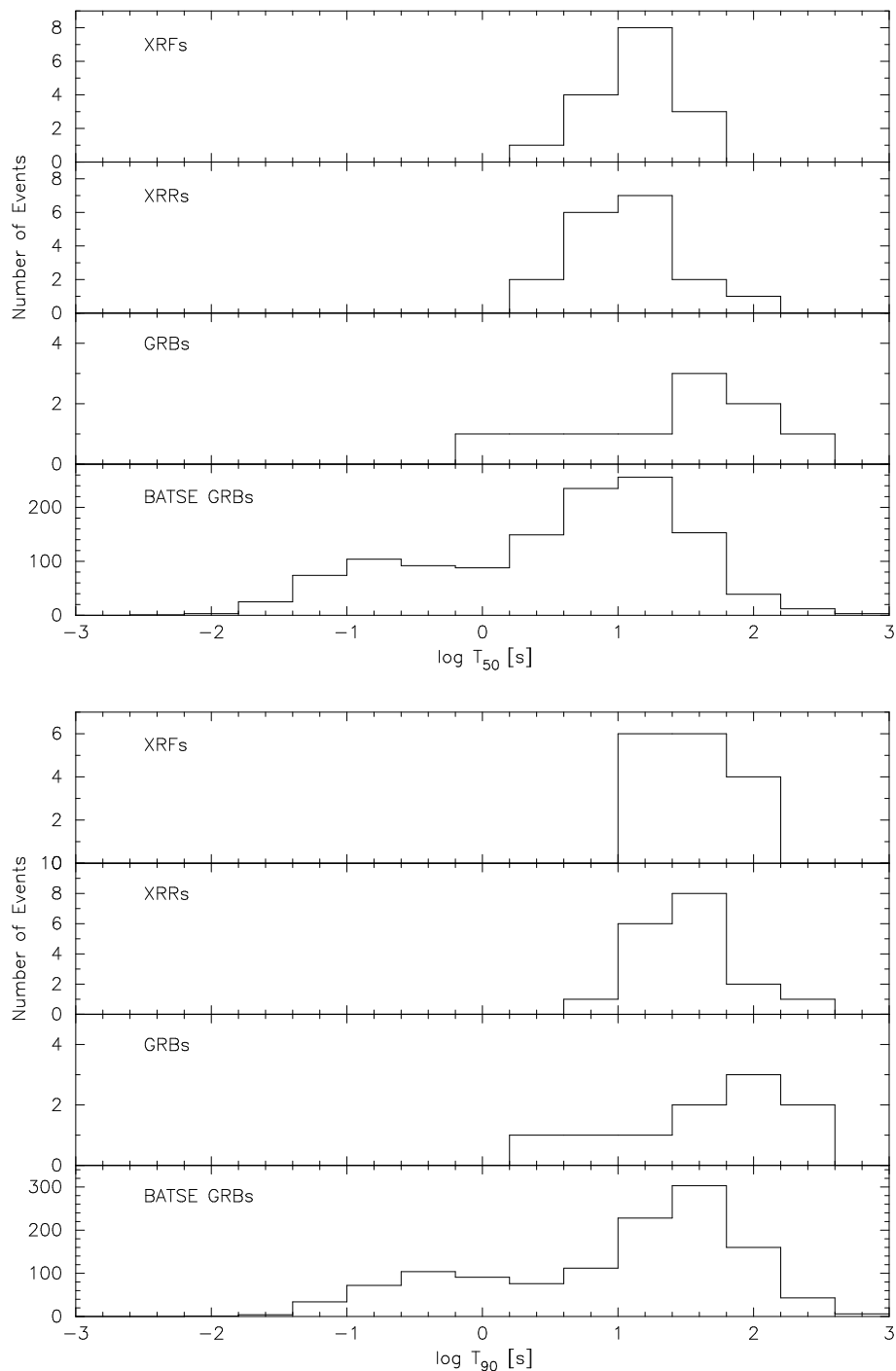


Fig. 3.— Comparison between T_{50} (top panel) and T_{90} (bottom panel) measures of burst duration in the 2–25 keV energy band for the three kinds of bursts seen by HETE-2 and in the 50–300 keV energy band for BATSE GRBs. The subpanels in the top and bottom panels shows (from top to bottom) the distribution of the durations of XRFs, XRRs, GRBs, and BATSE GRBs. The duration of BATSE sample includes not only the long GRBs but also the short GRBs.

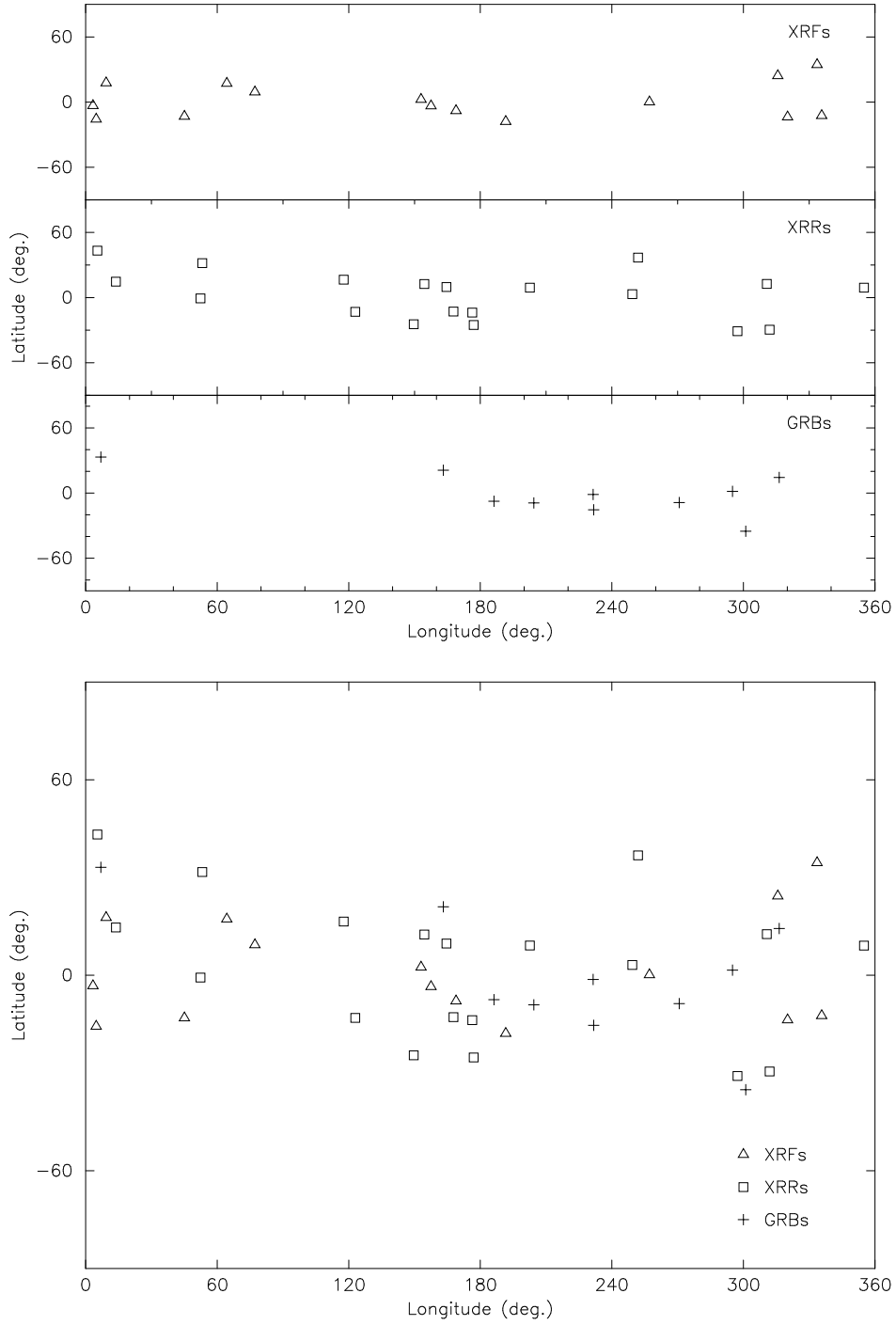


Fig. 4.— Comparison of the sky distributions in ecliptic coordinates of the HETE-2 XRFs, XRRs, and GRBs (top three panels), and for all of the bursts in this study (bottom panel).

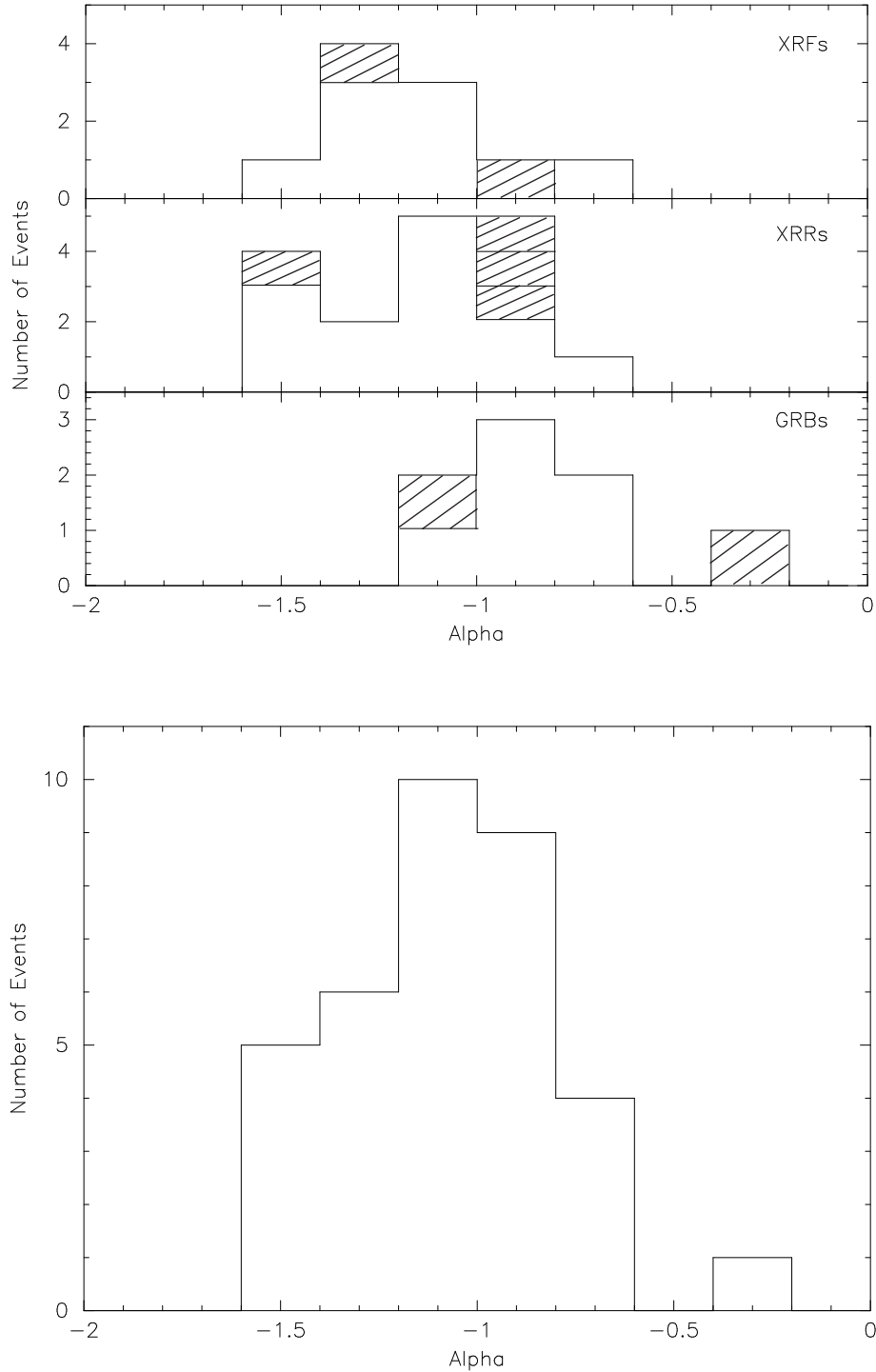


Fig. 5.— Distribution of the low-energy power-law index α for each of the three kinds of bursts (top panel) and for all of the bursts (bottom panel). The hatched α -values are the burst spectra requiring the Band model and the non-hatched α -values are the burst spectra that are adequately fit by the PLE model (top panel).

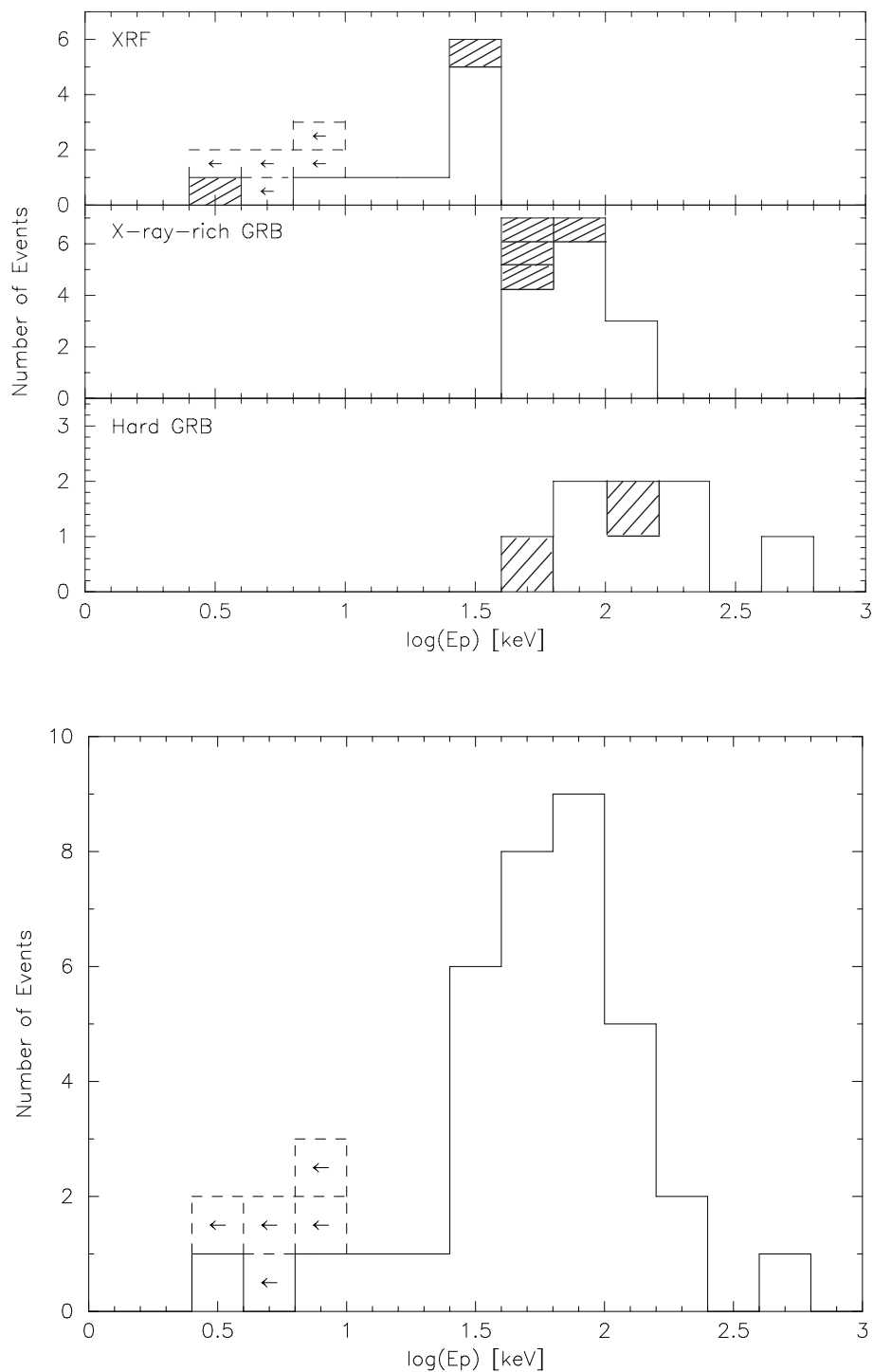


Fig. 6.— Distribution of E_{peak} for each of the three kinds of bursts (top panel) and for all of the bursts (bottom panel). The hatched E_{peak} -values are the burst spectra requiring the Band model and the non-hatched E_{peak} -values are the burst spectra that are adequately fit by the PLE model (top panel).

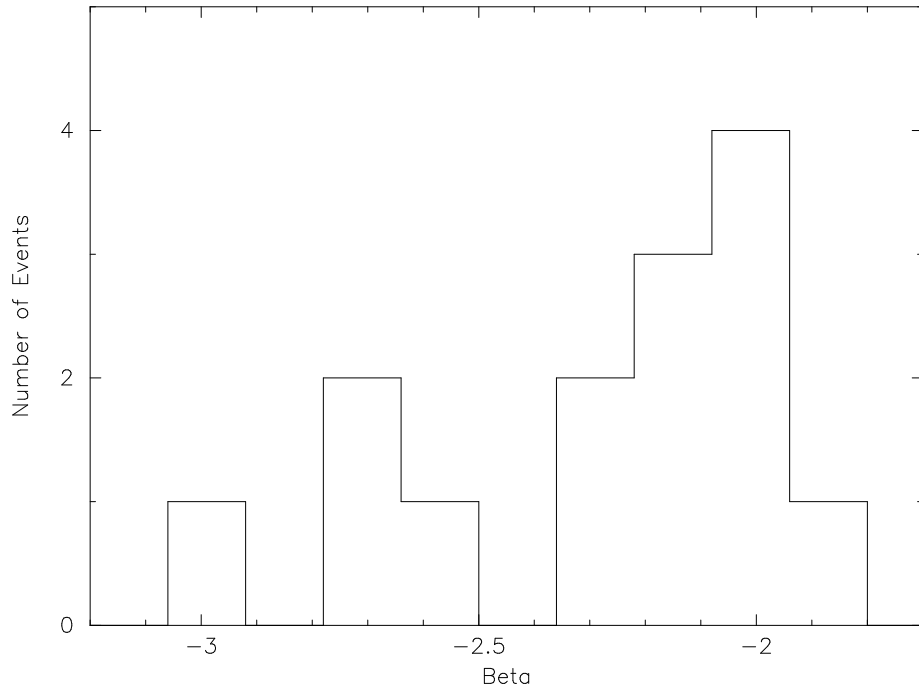


Fig. 7.— Distribution of the high-energy power-law index β for all of the bursts for which β could be determined. Two GRBs (GRB020813 and GRB030519) with $\beta > -2$ are not included in the sample, because they do not represent actual “peak” energy in νF_ν spectrum.

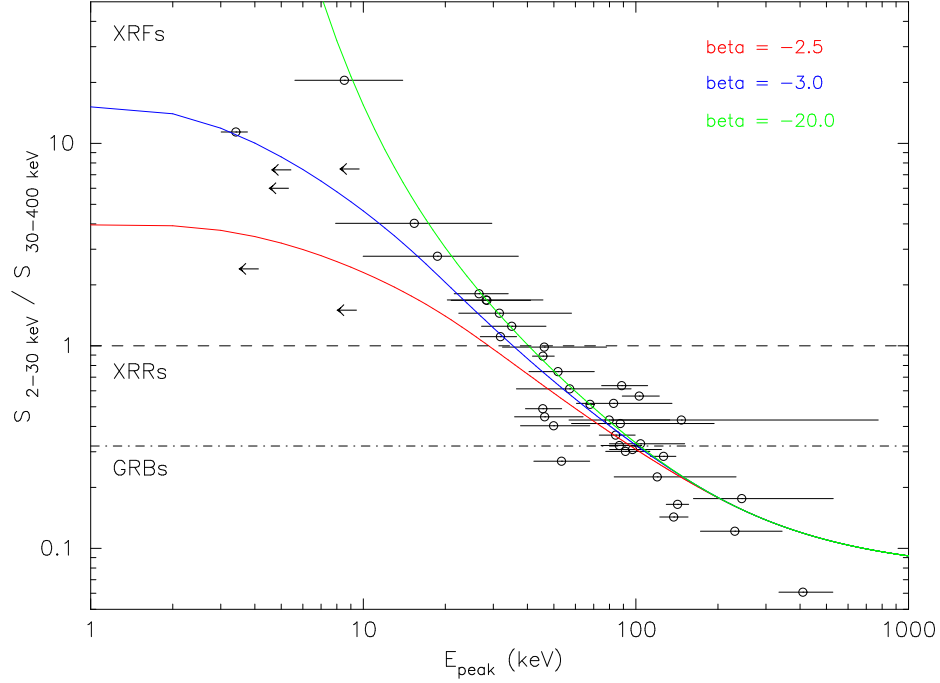


Fig. 8.— Distribution of bursts in the $[E_{\text{peak}}, S_E(2-30 \text{ keV})/S_E(30-400 \text{ keV})]$ -plane. Overlaid are curves corresponding to the X-ray to γ -ray fluence ratio as a function of $E_{\text{peak}}^{\text{obs}}$, assuming the Band function with $\alpha = -1$ and $\beta = -2.5$ (red), -3.0 (blue), and -20.0 (green).

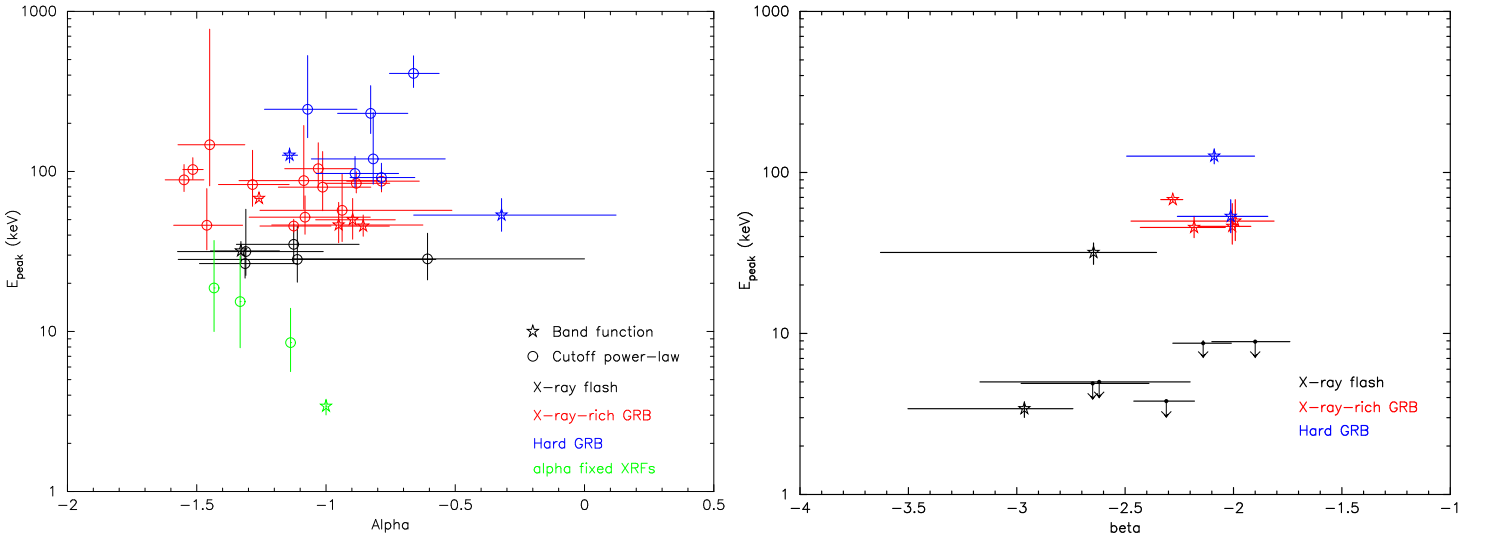


Fig. 9.— The low-energy power-law index α (left panel) and β (right panel) vs. $E_{\text{peak}}^{\text{obs}}$. The three kinds of bursts are denoted by different colors (XRF: black; XRR: red; and hard GRB: blue) and different symbols indicate the different best-fit spectral models (circle: PLE model; star: Band function). Also plotted are the XRFs for which the value of α was fixed (green).

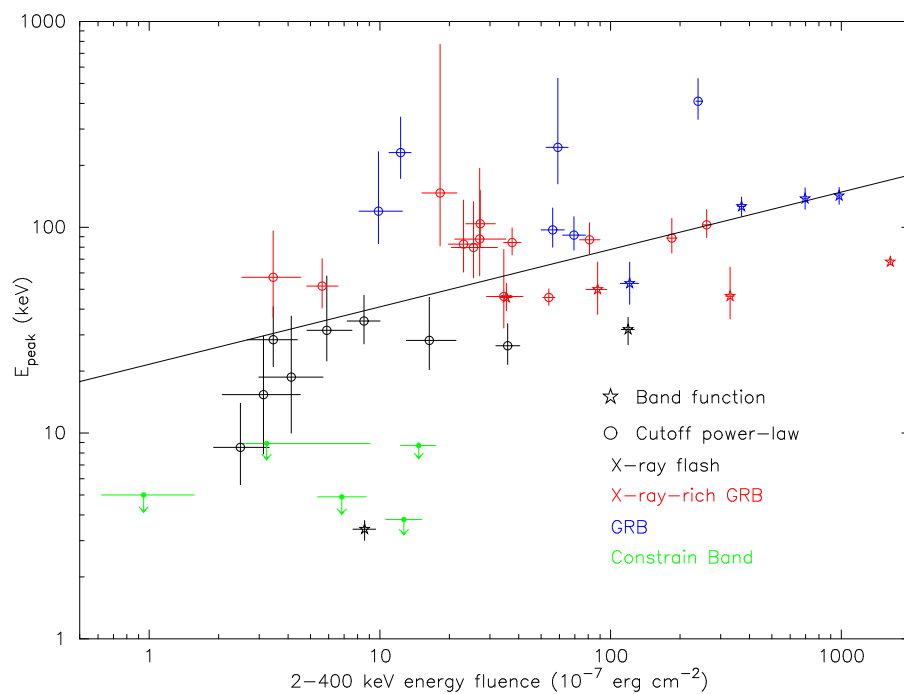


Fig. 10.— Distribution of bursts in the $[S_E(2-400 \text{ keV}), E_{\text{peak}}^{\text{obs}}]$ -plane. The solid line is the best linear fit to the burst distribution, and is given by $E_{\text{peak}}^{\text{obs}} = (21.577 \pm 4.656) \times [S_E(2-400 \text{ keV})/10^{-7} \text{ ergs cm}^{-2} \text{ s}^{-1}]^{0.279 \pm 0.053}$. The correlation coefficient for the burst distribution is 0.511.

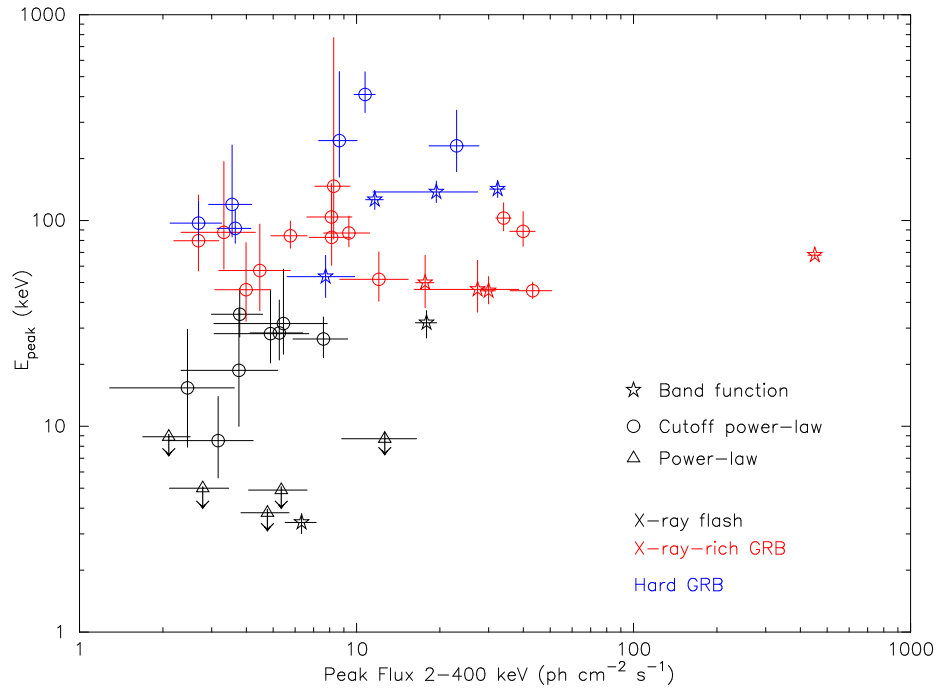


Fig. 11.— Distribution of bursts in the $[F_N^P(2-400 \text{ keV}), E_{\text{peak}}^{\text{obs}}]$ -plane. The correlation coefficient for the burst distribution is 0.297.

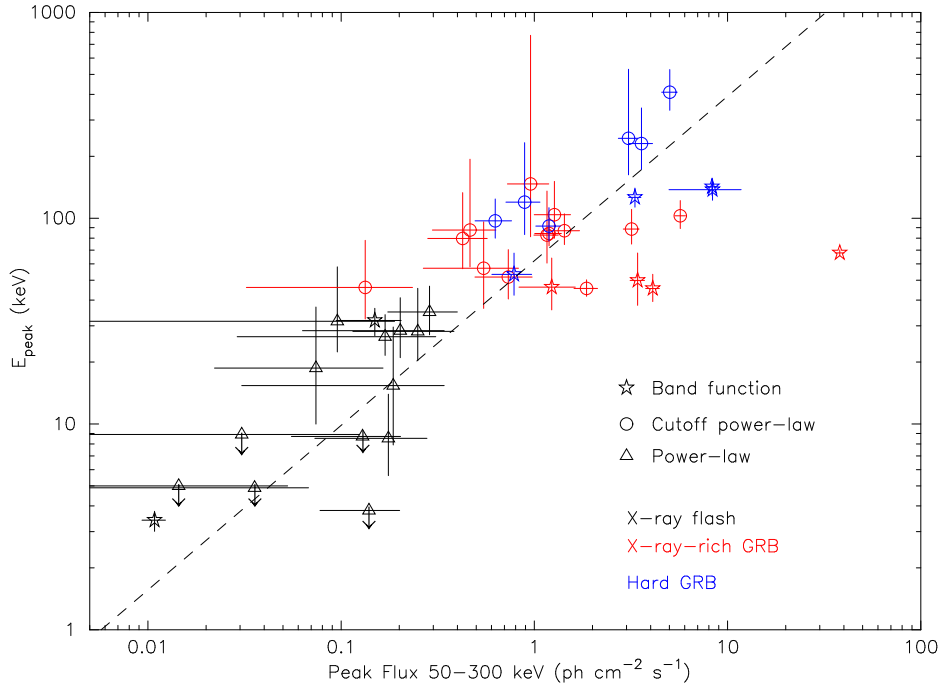


Fig. 12.— Distribution of bursts in the $[F_N^P(50-300 \text{ keV}), E_{\text{peak}}^{\text{obs}}]$ -plane. The dashed line corresponds to the best linear fit to the burst distribution and is given by $E_{\text{peak}}^{\text{obs}} = 62.02 \pm 1.71 F_N^P(50-300 \text{ keV})^{0.80 \pm 0.32}$. The correlation coefficient for the burst distribution is 0.802.

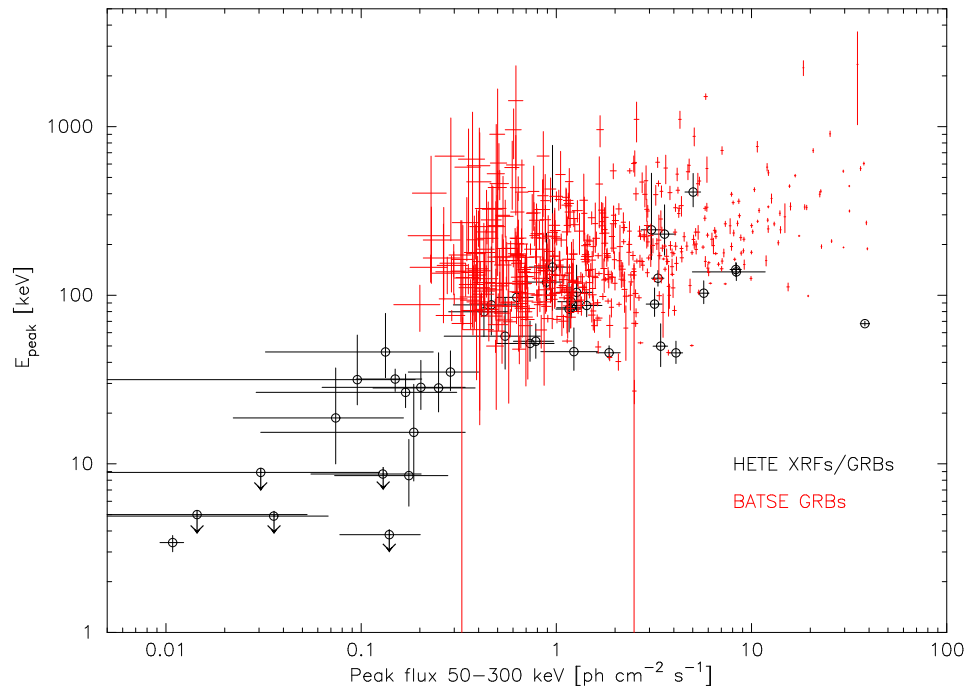


Fig. 13.— Distribution of HETE-2 bursts (black) and BATSE bursts (red) in the $[F_N^P(50\text{--}300\text{ keV}), E_{\text{peak}}^{\text{obs}}]$ -plane.

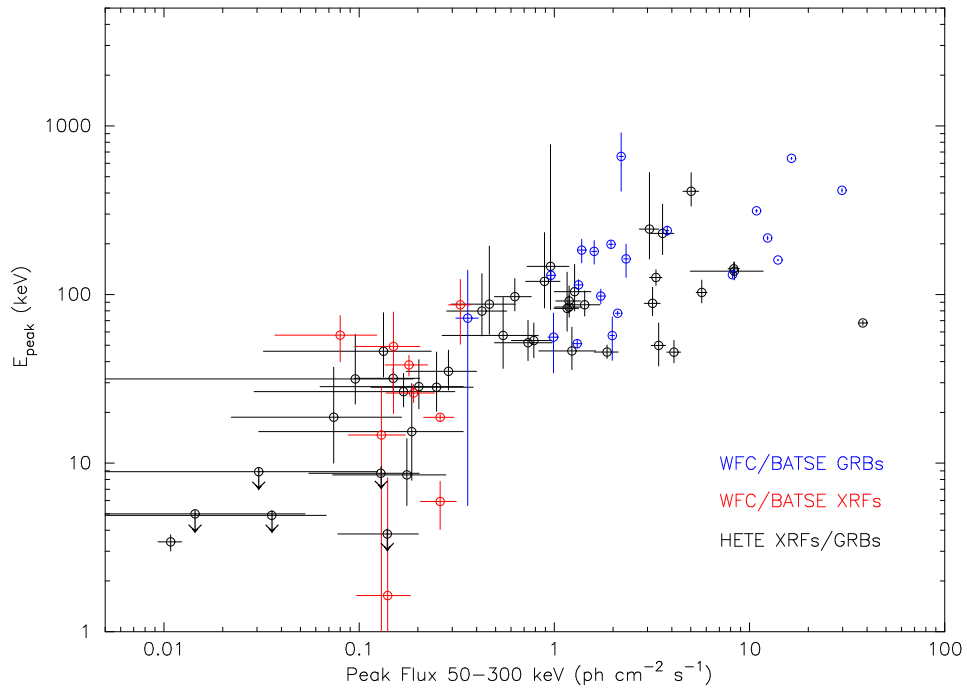


Fig. 14.— Distribution of HETE-2 bursts (black) and WFC/BATSE bursts (red and blue) in the $[F_N^P(50-300 \text{ keV}), E_{\text{peak}}^{\text{obs}}]$ -plane.

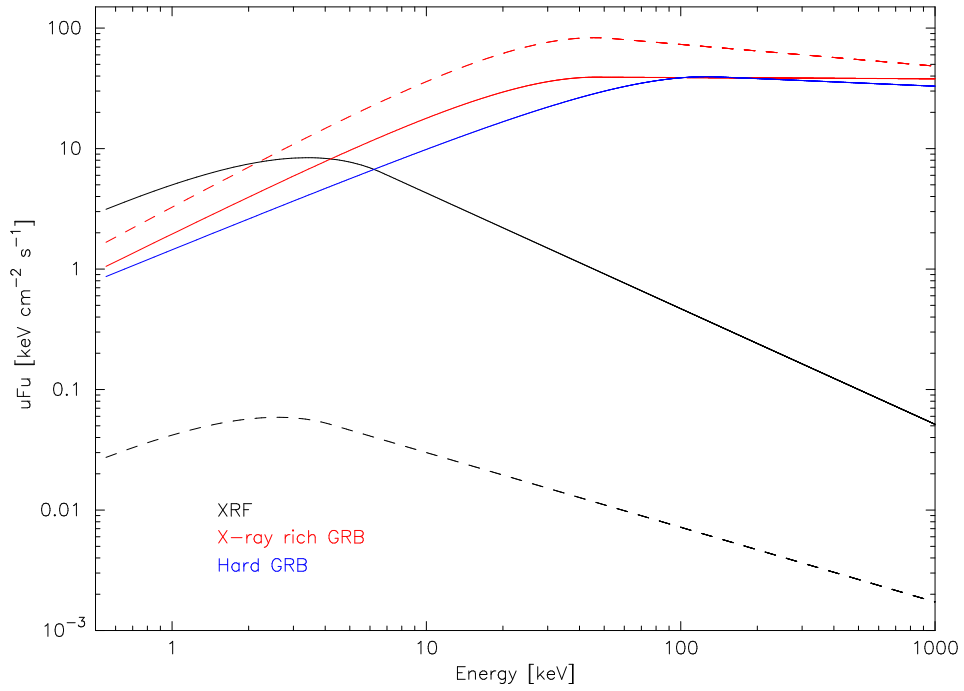


Fig. 15.— Examples of best-fit νF_ν spectra for XRFs (black) GRB010213 (solid) and GRB020903 (dash), XRRs (red) GRB010613 (solid) and GRB021211 (dash), and GRBs (blue) GRB030328 (solid).